Synthesis, Characterisation, Hirshfeld surface analysis, Magnetic susceptibility, DFT calculations, pkCSM profile, and Biological activities of Novel mono-, di-, and multinuclear Cobalt (II) complexes

Oussama Khaoua, Soumia Mouffouk, Noura Benbellat, Samira Zeroual, Stéphane Golhen, Abdelkrim Gouasmia, Henry Chermette, Hamada Haba

10.1002/ejic.202400033

RESEARCH ARTICLE

Synthesis, Characterisation, Hirshfeld surface analysis, Magnetic susceptibility, DFT calculations, *pkCSM* profile, and Biological activities of Novel mono-, di-, and multinuclear Cobalt (II) complexes

Oussama Khaoua,*[a] Soumia Mouffouk,[b] Noura Benbellat,*[a] Samira Zeroual,[a] Stéphane Golhen,[c] Abdelkrim Gouasmia,[d] Henry Chermette[e] and Hamada Haba[b]

[a] Dr. O. Khaoua, Pr. N. Benbellat, Dr. S. Zeroual.
Laboratoire de Chimie des Matériaux et des Vivants : Activité & Réactivité (LCMVAR), Département de Chimie, Faculté des Sciences de la Matière, Université de Batna-1, Algérie
E-mail: noura.benbellat@univ-batna.dz ; oussamakhaoua@univ-batna.dz

b] Dr. S. Mouffouk, Pr. H. Haba
Laboratoire de Chimie et Chimie de l'Environnement, Département de chimie (LCCE), Département de Chimie, Faculté des Sciences de la Matière, Université de Batna-1, Algérie

[c] Dr. S.Golhen
Université de Rennes, CNRS, ISCR (Institut des Sciences Chimiques de Rennes)-UMR 6226, F-35042 Rennes, France

[d] Pr. A. Gouasmia
Laboratoire des Matériaux Organiques et Hétérochimie, Faculté des Sciences et de la Technologie, Université Larbi Tébessi, Tébessa, Algérie

[e] Pr. H. Chermette
Institut des Sciences Analytiques de Lyon, UMR 5280 CNRS-Université Lyon 1, F-69622 Villeurbanne Cedex, France

Supporting information for this article is given via a link at the end of the document.

Abstract: This study explores the synthesis and diverse properties of newly synthesised water-soluble cobalt (II) complexes (**1**-**3**). Analysis of the complexes through various methods, including Hirshfeld surface analysis, reveals distinctive intermolecular interactions, particularly robust H-bonding contributions to crystal packing. 2D fingerprint plots provide quantitative insights into supramolecular interactions, while TGA-DSC analysis elucidates multi-step decomposition processes, mainly involving organic moieties. FT-IR and SCXRD confirm the structures of the complexes. Magnetic susceptibility measurements show paramagnetic behaviour in all complexes. FMO calculations expose HOMO-LUMO gaps and charge transfer processes, with NBO analysis emphasizing the significance of chloride, nitrogen, and oxygen atoms in coordination. In addition, pkCSM profile was carried out. The biological properties of the complexes reveal potent antibacterial activity for **2** and **3** against Gram-positive and Gram-negative bacteria. Despite lower antibacterial efficacy compared to standard antibiotics, their water solubility suggests potential human pharmacological applications. In terms of anti-inflammatory activity, all three complexes exhibit concentration-dependent prevention of ovalbumin denaturation, with **2** being the most effective. Compound **3**, despite having seven carboxyl groups, exhibits the weakest anti-inflammatory effect, potentially attributed to complex formation obscuring these groups. Furthermore, all complexes display antioxidant activities; **1** and **2** are greater than BHT in the ferric thiocyanate assay.

Introduction

Coordination chemistry has become a hot topic in recent studies notably those with organic ligands that contain heteroatoms as coordination sites, providing especially a large number of useful complexes with many potential applications such as antifungal, antibacterial, and anticancer properties [1–3], conductance fields [4–7], and magnetic exchange [8–11]. Five or six-membered heterocyclic compounds, such as isoquinoline and pyridine derivatives, featuring electron-donating nitrogen atoms, are well-recognised for their significance in coordination chemistry and biological systems, owing to their versatile chelating abilities [12]. In contrast, phenolic acids possess a unique structure extensively studied in numerous works due to their wide-ranging biological properties, encompassing antioxidant, anti-inflammatory, antimicrobial, antimutagenic, and anticancer effects [13,14], and find application as pharmacophores in medicinal chemistry, notably in non-steroidal anti-inflammatory drugs like diclofenac, ibuprofen, and fenclofenac [15,16]. Also, isoquinoline and quinoline derivatives serve as compelling targets for DNA-Gyrase [17,18]. Additionally, metals play a crucial role as essential drugs in 50-70% of all cancer chemotherapy [19,20]. Previous studies have highlighted the efficacy of metals such as titanium, gold, and vanadium and their complexes as anticancer agents for conditions like breast cancer [21–24]. Clinically, three platinum complexes; platinum, oxaliplatin, and cisplatin *cis*-$[Pt(NH_3)_2Cl_2]$, the latter marketed since 1978 have been extensively utilised [25]. A second

example concerns cobalt, an essential metal found in very low abundance in the human body, which primarily exists as Cobalt (I-IV) [26], plays an important biochemical role in DNA synthesis and regulation; it is a component of vitamin B12, involved in fatty acid metabolism. Numerous reports on the properties of cobalt (II)–based complexes appear in the literature, encompassing antibacterial effects, therapeutic uses as a tumour imaging agent, involvement with transport protein transferrin, antitumour, antiparasitic, enzymatic therapeutics, antifungal, and anti-inflammatory activities [27–31]. Accordingly, the present work focuses on the synthesis and characterisation of three novel cobalt (II) mixed and non-mixed ligand complexes, including a mononuclear isoquinoline (Isoq) complex containing two units $[Co(Isoq)_4Cl_2]0.5H_2O$ (Co1 and Co2) **1**, a binuclear complex $[Co_2(DMAP)_2(\mu\text{-}Benz)_4]$ **2** based on mixed ligands (benzoate (Benz) and dimethyl aminopyridine (DMAP)), and a trinuclear benzoate complex bridged by water molecules $[Co_3(Benz)_4(\mu\text{-}Benz)_4.(H_2O)_4]$ **3**. These compounds **(1-3)** were isolated and characterised using single-crystal X-ray diffraction, FT-IR, and UV-Vis. Furthermore, detailed discussions on their thermal TGA-DSC and magnetic properties are provided. DFT calculations were conducted using the B3LYP/6-311G(d,p) level of theory to gain a better understanding of their experimental properties. The frontier orbitals and molecular electrostatic potentials of the title compounds were calculated. Additionally, important interactions and closest contacts between the active atoms, including hydrogen bonding and hydrophobic interactions, were identified through Hirshfeld surface analysis. This theoretical approach facilitates the interpretation of the antimicrobial activities tested against six micro-organisms, including five bacterial strains (*Staphylococcus aureus* (*S. aureus*), *Escherichia coli* (*E. coli*), *Pseudomonas aeruginosa (P.aeruginosa), Klebsiella pneumonae* (*K. pneumonae*)*, and Streptococcus* (*sp*)) and one fungus (*Candida albicans* (*C. albicans*))*.* Additionally, the antioxidant and anti-inflammatory activities were assessed.

Experimental

PREPARATION OF METAL COMPLEXES

Synthesis of Dichlorotetra-isoquinolinecobalt (II)-0.5hydrate 1 $[Co(Isoq)_4Cl_2].0.5H_2O$

Complex **1** was obtained as follows: (240 mg, 1 mmol) $CoCl_2.6H_2O$ in 20 mL ethanol/distilled water (2:1) mixture was stirred vigorously for 20 min. (0.24 mL, 2 mmol) of isoquinoline was added dropwise to the solution for another 20 min. The mixture was then left at room temperature for 2.5 h with vigorous stirring. After five days, before the complete evaporation of the solvent mixture, needle-shaped pink crystals suitable for X-ray diffraction were obtained. Yield: 0.323 g (26%). Mp: 200 °C.
IR data (ATR, υ/cm^{-1}): 3350–3200 [υOH] (water molecules); 3089–2919 [υArH], 1609 [υC=C], 1590 [υ_{sy}C=C], 1508, 1455, 1413 [υCN], 1367, 1250 [υ_{asy}C=C], 1238, 1168 [υC–C], 1108, 1037 [δCH] (In the plane), 989 [δCH] (Out of the plane), 904, 836 [υCo–Cl], 725, 698, 539, 491 [υCo–N].
UV-Vis data (λ_{max}, EtOH, nm): 213, 236, 245, 263, 276 (π→π*), 312 (n→n*), 517 (d→d).

Synthesis of Tetrakis(μ-benzoato) bis{[4-(dimethylamino)-pyridine] cobalt (II) 2 $[Co_2(DMAP)_2(\mu\text{-}Benz)_4]$

Complex **2** was prepared as follows: a mixture of $CoCl_2.6H_2O$ (240 mg, 1 mmol) and benzoic acid (241 mg, 2 mmol) in 13 mL absolute ethanol. The mixture was stirred at room temperature for 30 min. While stirring, (244.3 mg, 2 mmol) of N,N-dimethyl-4-aminopyridine, which has been dissolved in 7 mL of distilled water (warmed slightly and stirred gently to dissolve the ligand), was slowly added to the ethanoic solution over 20 min. The final mixture was vigorously stirred for 2 h. After that, the formed precipitate was filtered and removed. After a few days of slow evaporation of the liquid mixture at room temperature, dark black single crystals were obtained and washed with a minimal amount of cold absolute ethanol/distilled water and air-dried. Yield: 0.223 g (14%). Mp: 264 °C.
IR data (ATR, υ/cm^{-1}): 3214 [υOH] (water molecules), 3057-2925 [υArH], 1610 [υC=C], 1566 [υ_{sy}C=C], 1535, 1438 [υCN], 1397, 1286 [υC–O], 1228, 1174, 1114, 1016 [δCH] (In the plane), 948 [δCH] (Out of the plane), 839, 813, 718, 689, 676, 576, 548, 528, 506, 459 [υCo–N], 432 [υCo–O].
UV-Vis data (λ_{max}, EtOH, nm): 201, 216 (π→π*) 259 (n→n*), 568 (d→d).

Synthesis of Tetrakis-(μ-benzoato) bis-[(Co(1), Co(3)-Benzoate] tetra-aqua tricobalt (II) 3 $[Co_3(Benz)_4(\mu\text{-}Benz)_4.(H_2O)_4]$

Complex **3** was prepared by reacting 2:1 stoichiometric ratio of the benzoate ligand and Co salt, at room temperature. $CoCl_2.6H_2O$ (238 mg, 1 mmol) was solubilized in 13 mL of absolute ethanol. Under stirring, a solution of 240 mg (2 mmol) of benzoic acid in 7 mL of distilled water was added over 20 min. The mixture was kept under live stirring for 2.5 h. An aggregate of dark pink single crystals precipitates after few days of slow evaporation. The formed crystals were collected, filtered off, washed thoroughly with a minimum amount of cold absolute ethanol/distilled water mixture, and finally air-dried at room temperature. Yield: 0.192g (8%). Mp: 266 °C.
IR data (ATR, υ/cm^{-1}): 3242 [υOH] (water molecules), 3056-2925 [υArH], 1647 [υC=O], 1608 [υC=C], 1565 [υC=C], 1441 [υCN], 1385, 1212, 1175 [υC–C], 1138, 1069 [υC–O], 1023 [δCH] (In the plane), 998 [δCH] (Out of the plane), 940, 883, 819, 797, 719, 691, 674, 575, 529, 503, 440 [υCo–O].
UV-Vis data (λ_{max}, EtOH, nm): 201, 223 (π→π*) 260, 279 (n→n*), 568(d→d).

ANTIMICROBIAL ACTIVITY

The cobalt (II) complexes **1-3** were tested for their antimicrobial activities using the agar disk diffusion method, against five bacterial strains including two Gram-positive (*Staphylococcus aureus* ATCC 25923 and *Streptococcus* ATCC) and three Gram-negative (*Escherichia coli* ATCC 25922, *Pseudomonas aeruginosa* DMS 1117 and *Klebsiella pneumoniae*) as well as one fungi strain (*Candida albicans* ATCC 90029) [32]. In 5 mL of nutrient broth, one or more colonies were dissolved until the cells in suspension reached the turbidity of the 0.5 McFarland standard. Bacterial inoculate were smeared on the surface of Muller Hinton agar using a sterile swab. In addition, discs of Whatman paper with a diameter of 6 mm were cut out and sterilised in an autoclave then soaked with 10 µL of the

various concentrations (10, 5, 2.5, 1.25, and 0.625 mg/mL) of the samples and carefully deposited on the surface of the inoculated agar with sterile forceps. DMSO was used as negative control while penicillin and gentamicin were utilised as positive control. Prepared dishes were incubated at 37 °C for 24 hours. The antibacterial activity was assessed by measuring the diameters of the zones of inhibition in millimetres (mm) and the values were expressed as the mean ± SD of three trials ($p < 0.05$). To estimate antifungal activity, the same experimental method for antibacterial activity was involved using Sabouraud's agar. However, Petri dishes were incubated at 30 °C for 72 hours.

EGG ALBUMIN DENATURATION METHOD

The *in vitro* anti-inflammatory effect of metal complexes **1**, **2**, and **3**, was tested using the egg albumin denaturation technique [33]. Briefly, 2 mL of different concentrations of the tested complexes or reference drug were added to a mixture of 200 µL of egg albumin (from fresh hen's egg) and 2.8 mL of phosphate-buffered saline (PBS, pH 6.4). The resulting solutions were incubated for 15 minutes at 37 °C and, then heated for 5 minutes at 70 °C. The absorbances were read at 660 nm and the percentages of inhibition of protein denaturation were measured by the following formula:

$$\% \text{ inhibition} = 100 \times [(V_S / V_C) - 1]$$

Where V_S: absorbance of the sample, Vc: absorbance of control.

ANTIOXIDANT ACTIVITIES

DPPH FREE RADICAL-SCAVENGING ASSAY

The antioxidant activity of Co^{II} complexes $[Co(Isoq)_4Cl_2]$ $0.5H_2O$ **1**, $[Co_2(DMPA)_2(\mu\text{-Benz})_4]$ **2**, and $[Co_3(Benz)_4(\mu\text{-Benz})_4.(H_2O)_4]$ **3** was estimated using the free radical DPPH [34]. Indeed, 25 µL of different dilutions of the samples (complexes or standards) were added to 975 µL of DPPH (0.025 mg/mL) prepared in methanol. The resulting mixture was kept in a dark place for 30 minutes at room temperature. The absorbances were measured at 517 nm. The percentage of inhibition of each sample was calculated as follows:

$$I\% = [(A_{Blank} - A_{Sample}) / A_{Blank}] \times 100$$

A_{Blank} is the absorbance of the blank and A_{Sample} is the absorbance of the sample.

TOTAL ANTIOXIDANT CAPACITY

The total antioxidant capacity of Co^{II} complexes was evaluated by the phosphomolybdenum method [32]. 100 µL of samples were combined with 900 µL of reagent solution (0.6 M sulfuric acid, 28 mM sodium phosphate, and 4 mM ammonium molybdate). The prepared tubes were incubated for 90 minutes at 95 °C. After cooling at room temperature, the absorbances were taken at 695 nm against a blank. The antioxidant capacity of samples was expressed as µg equivalents of ascorbic acid per mg of complex (µg of EAA/ mg of the complex).

FERRIC THIOCYANATE ASSAY

To estimate the quantity of peroxide produced over the initial stages of lipid oxidation, the ferric thiocyanate assay was performed on the metal complexes (**1**, **2**, and **3**), as well as the reference molecules (BHA, BHT, ascorbic acid, and quercetin) by the method described by Takao et al. [35]. The reaction mixture containing 400 µL of samples (Co^{II} complexes or standards) at the concentration of 100 µg/mL, 400 µL of linoleic acid, and 800 µL of phosphate buffer (pH 7.4) was incubated for 1 hour at 40 °C. An aliquot of 100 µL of the resulting solutions was added to 5 mL of ethanol (70 %) and 100 µL of ammonium thiocyanate (30%). After 3 min, 100 µL of $FeCl_2$ prepared in hydrochloric acid (3.5%) were added to the mixture. The absorbances were read after 7 days at 500 nm. The percentage of inhibition of the lipid peroxidation was calculated according to the following equation:

$$\text{Inhibition (\%)} = (1- (A_{Sample} / A_{Blank})) \times 100$$

Results and Discussion

CRYSTAL STRUCTURES DESCRIPTIONS

Compound (**1**) crystallises in the centrosymmetric monoclinic $P2_1/n$ space group, with two $[Co(Isoq)_4Cl_2]$ complexes (Co1 and Co2) and one water solvent per asymmetric unit. One isoquinoline ligand of one cobalt complex is disordered (Figure 1). During refinement, the isoquinoline ligand from Co1, bearing N4 atom revealed large anisotropic displacement parameters. Another isoquinoline (labelled B) was found close to the first one (labelled A), isoquinolines A and B are quite coplanar (the mean angle between the two planes built with the ten atoms of isoquinoline is 2.8(4)°) but twisted from 180° and with an angle N4B-Co1-N4A of 17.2(2)°. The occupation factors of isoquinoline fragments A and B were refined as free variables for A and (1-free variable) for B and found close to 0.5. For the last refinements, occupation factors were fixed to 0.5 for both A and B isoquinolines. The occupation factor for the water solvent molecule is found and then fixed to be equal to 0.5. The two chlorides are in trans position for the two complexes (Cl-Co-Cl being 179.89(8)° and 179.86(6)° for Co1 and Co2, respectively), whereas the isoquinoline planes in trans position form angles close to 90° (see table 1).

Table 1. Selected angles [°] for complex **1**

Angles	Angles values	Angles	Angles values
N1/N3	87.4(1)°	N5/N7	85.2(1)°
N2/N4A	88.1(3)°	N6/N8	85.6(1)°
N2/N4B	85.4(3)°		

10.1002/ejic.202400033

RESEARCH ARTICLE

Contacts involving the water molecule are 3.12 (2) Å with Cl3 of Co2 complex and 2.5084 Å with H13 belonging to Co2 complex. The short O1W - O1W (1-x, 1-y, 1-z) contact of 2.41(3) Å must be taken with caution as the occupation factor of water molecule is 0.5.

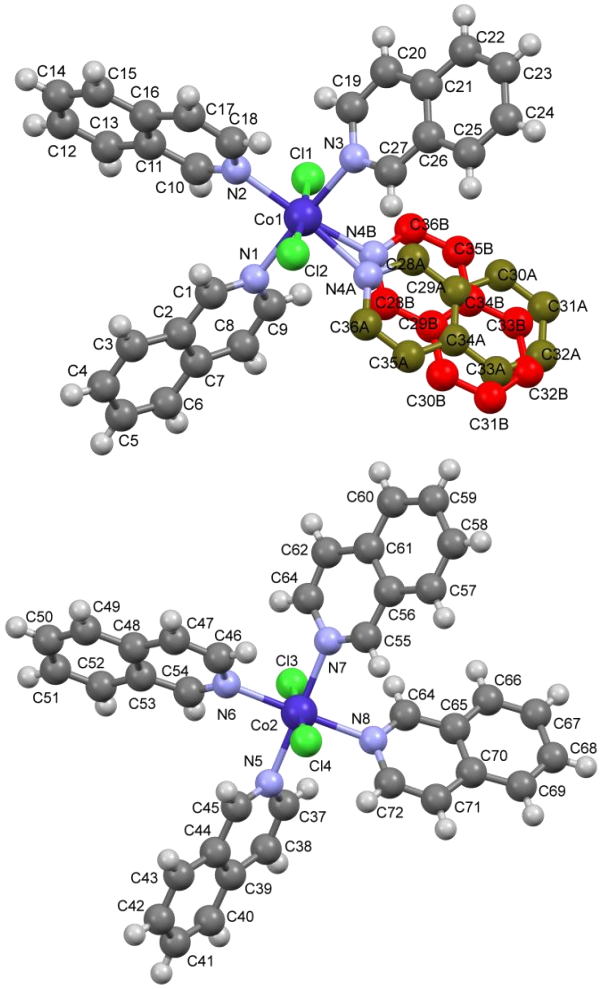

Figure 1. Labelling scheme of compound **2**, showing the disorder of isoquinoline ligand labelled "A" and "B" for complex Co1

An isotype of compound **2**, containing zinc ion, was previously described by Yu et al. [36]. Our cobalt compound crystallises in the centrosymmetric monoclinic $P2_1/n$ space group, consisting of one tetragonal dicobalt paddlewheel, where the four μ-benzoate ligands act as paddles and the axis consists of two aminopyridines. The labeling scheme for the compound is given in Figure 2. The benzoate's phenyl rings and carboxylate part are quite planar, with angles being 3.7(3)° and 14.8(2)° for benzoate with O1-C1-O2 and O3-C8-O4, respectively. Nevertheless, the paddlewheel is distorted as the carboxylate part of two adjacent paddles forms an angle of 85.6(2)° and the axis N1-Co…Co^{i} forms an angle of 154.61(4)°. The Co-Co contact in the paddlewheel is measured at 2.8360(5) Å. Figure 3 provides a view of the paddlewheel. The shortest intermolecular contact involving non-hydrogen atoms is larger than 3.4 Å which indicates that the molecule is relatively isolated.

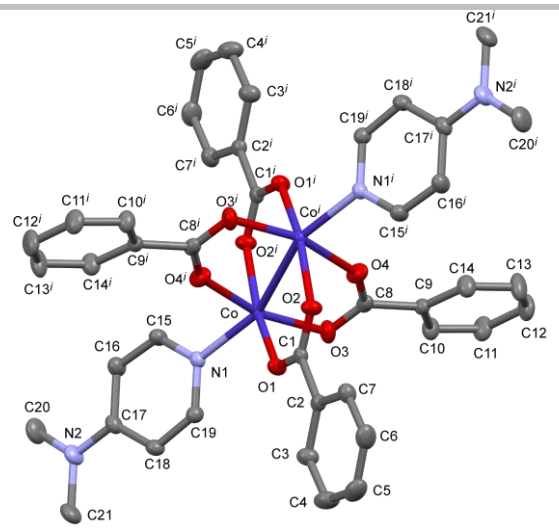

Figure 2. Labelling scheme of compound **2** with symmetry i: -x, 1-y, 1-z

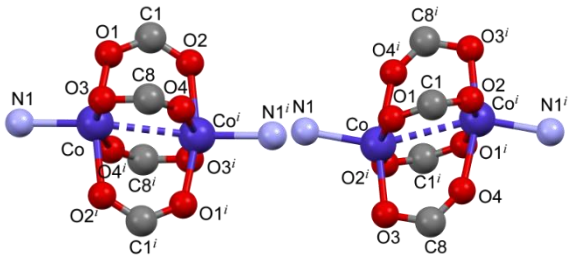

Figure 3. View of the distorted cobalt paddlewheel of compound **2** with symmetry i: -x, 1-y, 1-z

Compound **3** crystallises in the centrosymmetric triclinic P-1 space group. It consists of two independent centrosymmetric cobalt (II) trimers, the central cobalt ions (Co1 and Co4) of each trimer lying on an inversion centre, two cobalt (Co2 and Co3) in general position, each cobalt being coordinated with bridging or terminal oxygen atoms from benzoate ions and water molecules. Each cobalt ion lies in an octahedral oxygen coordination sphere (Figure 4). Four free benzoate ions and water molecules are also present in the structure.

RESEARCH ARTICLE

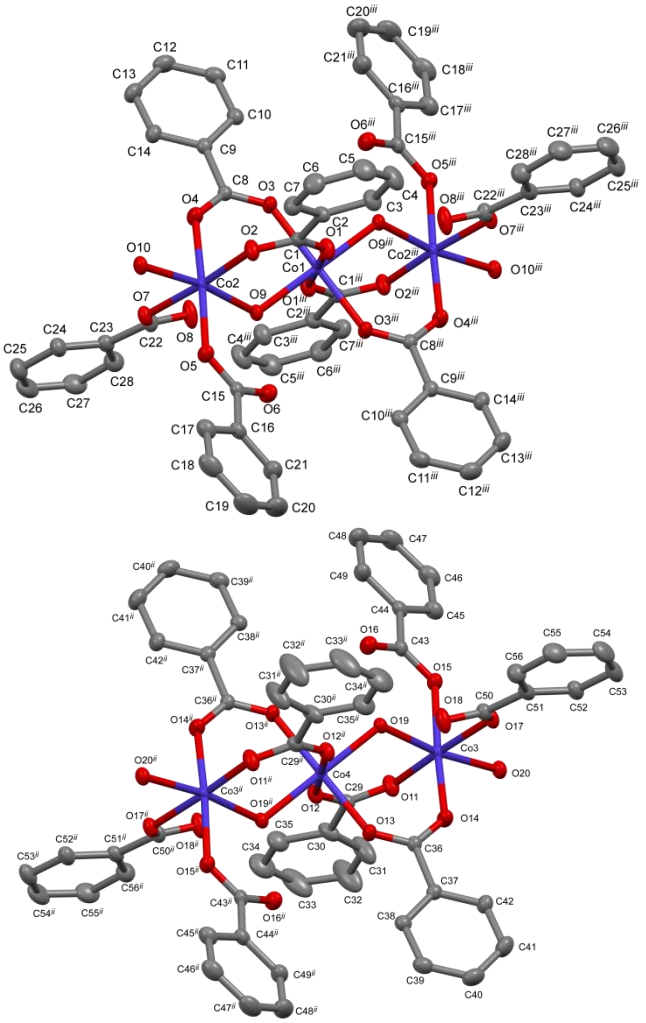

Figure 4. Labelling scheme of compound **3** with symmetries ii: 1-x, -y, 2-z and iii: 2-x, 1-y, 1-z

Non-centrosymmetric cobalt ions Co2 and Co3 coordination sphere is built to four oxygen atoms in an equatorial plane. Two oxygen atoms (O2, O4 and O11, O14, respectively) are derived from two $\mu_2(\eta_1\text{-}\eta_1)$ benzoate ions in cis position and two oxygen atoms (O5, O7 and O15, O17, respectively) from μ_1 benzoate ions in the remaining cis position. The apical positions are occupied by one bridging oxygen atom (O9 and O19) and one terminal oxygen atom (O10 and O20) from water molecules. The cobalt ions Co1 and Co4, located at the inversion centre, are respectively coordinated to two oxygen atoms O1 and O3 (O12 and O13) from two $\mu_2(\eta_1\text{-}\eta_1)$ benzoate ions and one bridging oxygen O9 (O19) from one water solvent molecule. The two complexes are quite similar as shown in Figure 5, with the complex containing Co1 and Co2 drawn in blue and the one with Co3 and Co 4 drawn in red. The main difference between the two phenyl rings is their mean planes (C2-C3-C4-C5-C6-C7 and C30-C31-C32-C33-C34-C35), which have an angle of 7.7° between them.

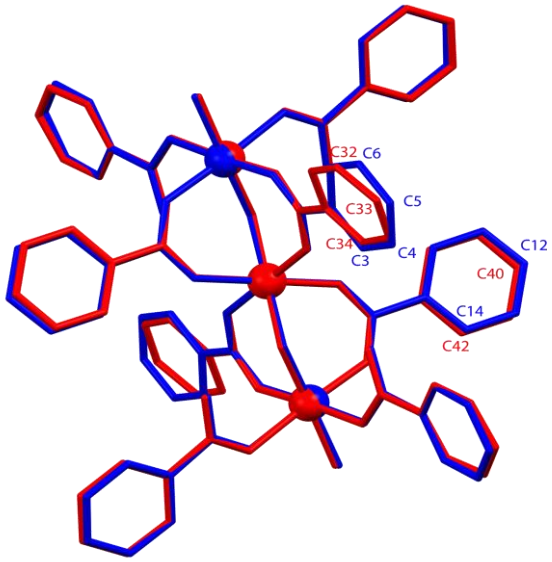

Figure 5. View of an overlay of the trinuclear complex involving Co1 and Co2 in blue and trinuclear complex involving Co3 and Co4 in red

The crystal structure consists of independent trimers Co2-Co1-Co2 and Co3-Co4-Co3 that alternate along the [1 1 -1] direction. This is made possible by inter-trimers hydrogen bond type contacts O17…H2T-O10 and O7…H4T-O20 with O17…O10 = 2.774(3) Å and O7…O20 = 2.761(3) Å (Figure 6). The asymmetric unit contains one water molecule (O1w) and two free independent benzoate ions, with one being disordered in two positions labelled A with 68% occupation factor (see atoms labelled O23A and O24A) and labelled B (see atoms labelled O23B and O24B) with 32% occupation factor. The other benzoate ions occupy a full general position (see O21 and O22)

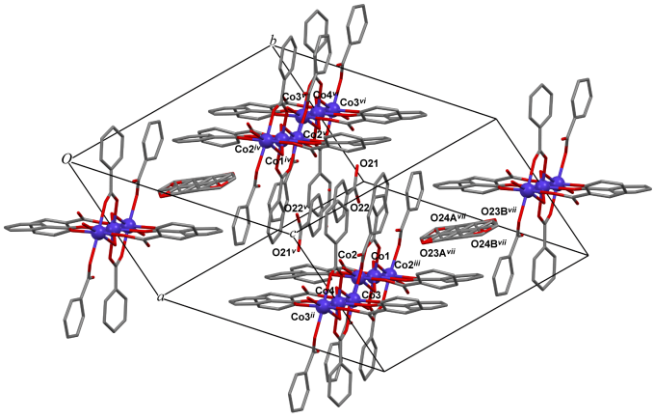

Figure 6. Packing of cobalt trimers complexes along [1 1 -1] direction in compound **3** with symmetries ii: 1-x, -y, 2-z; iii: 2-x, 1-y, 1-z; iv: x-1, y, z; v: 1-x, 1-y, 1-z; vi: x, 1+y, z-1; vii: x, 1+y, z

HIRSHFELD SURFACE ANALYSIS (HSA)

To explore and visualise the nature of interactions between molecules in the molecular structures of the obtained crystals, Hirshfeld surfaces (HS) [37–39] and 2D fingerprint maps [40–42] were investigated using Crystal Explorer software [43]. This

RESEARCH ARTICLE

software provides a powerful tool to quantify and gain insight into the different types of intermolecular interactions in complexes by setting spherical atomic electron densities [44,45]. The 3D Hirshfeld surfaces were plotted based on the normalised contact distance (d_{norm}), shape index (s), and curvedness. The d_{norm} was defined by the inside (d_i), the outside (d_e) distances, and the van der Waals radii of the atoms (r_i^{vdw} and r_e^{vdw}) using the following equation (Eq.1):

$$d_{norm} = \left(d_i - r_i^{vdw}\right)/r_i^{vdw} + \left(d_e - r_e^{vdw}\right)/r_e^{vdw} \qquad \text{(Eq.1)}$$

The 3D HS graphic uses a colour scheme of blue, white, and red. The blue regions represent longer contacts (with distances greater than the sum of the van der Waals radii), the white regions represent contacts around the van der Waals distance (with distances close to the sum of the van der Waals radii), and the red regions emphasise shorter contacts (distances less than the sum of the van der Waals radii) [46–49]. The dark red spots highlight the strong hydrogen bonding points in the crystal. The small size of this region and the light colour of the surface indicate weaker and longer contacts than hydrogen bonds. Complementary 2D fingerprints provide quantitative information on the individual contributions of such supramolecular interactions in crystal packing. In these interactions, one molecule acts as the donor ($d_e > d_i$) and the other acts as the acceptor ($d_e < d_i$). Figures illustrated by follow (Figure 7), show a view of the three-dimensional HS of compounds **(1-3)** plotted with the normalised contact distances (d_{norm}) over the range -0.3144 to 1.6157 a.u, -0.1259 - to 1.4686 a.u, and -0.6086 to 1.7633 a.u, respectively.

Their curvedness and shape indexes are also presented in the range of -4.000 to 0.400 a.u and -1.000 to 1.000 a.u, respectively.

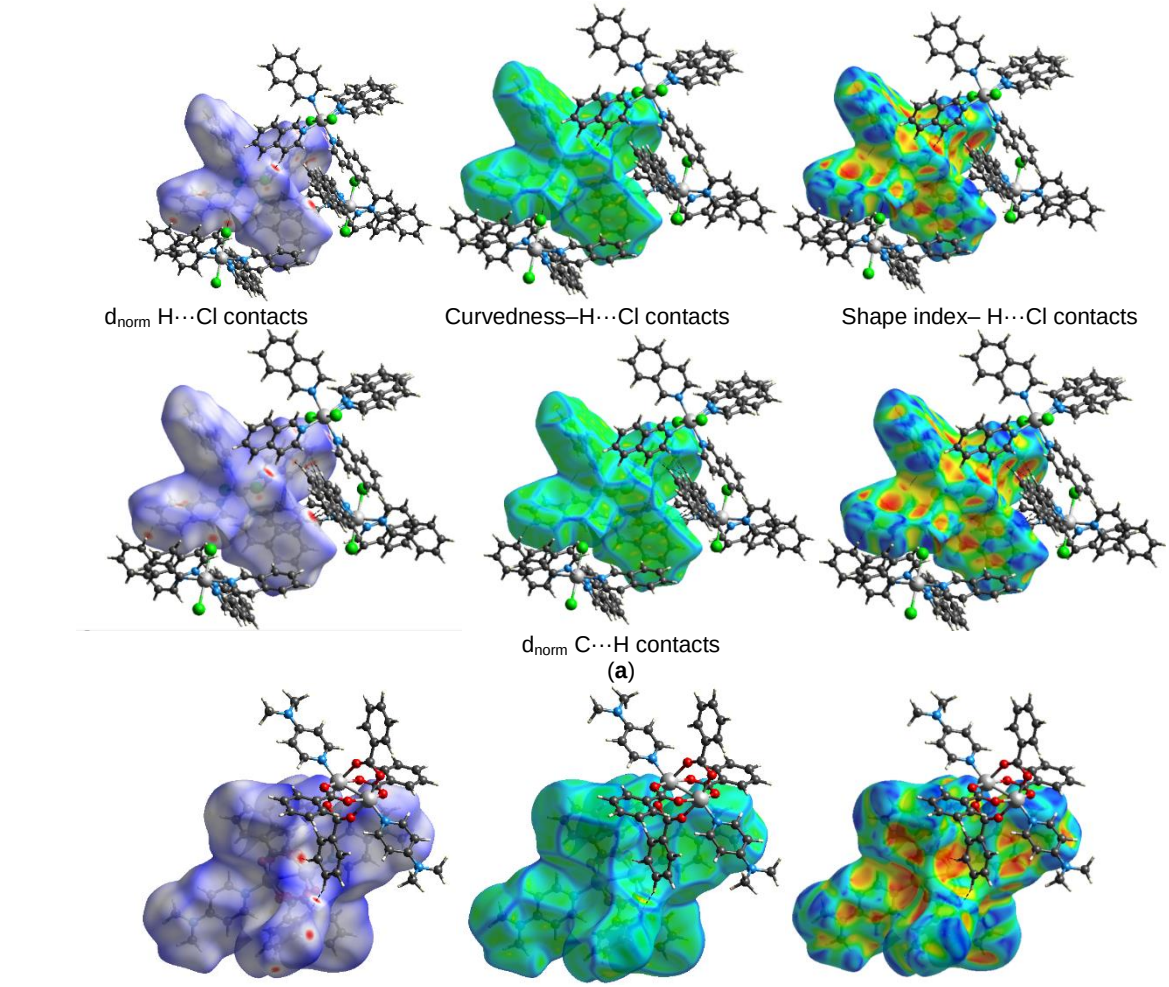

RESEARCH ARTICLE

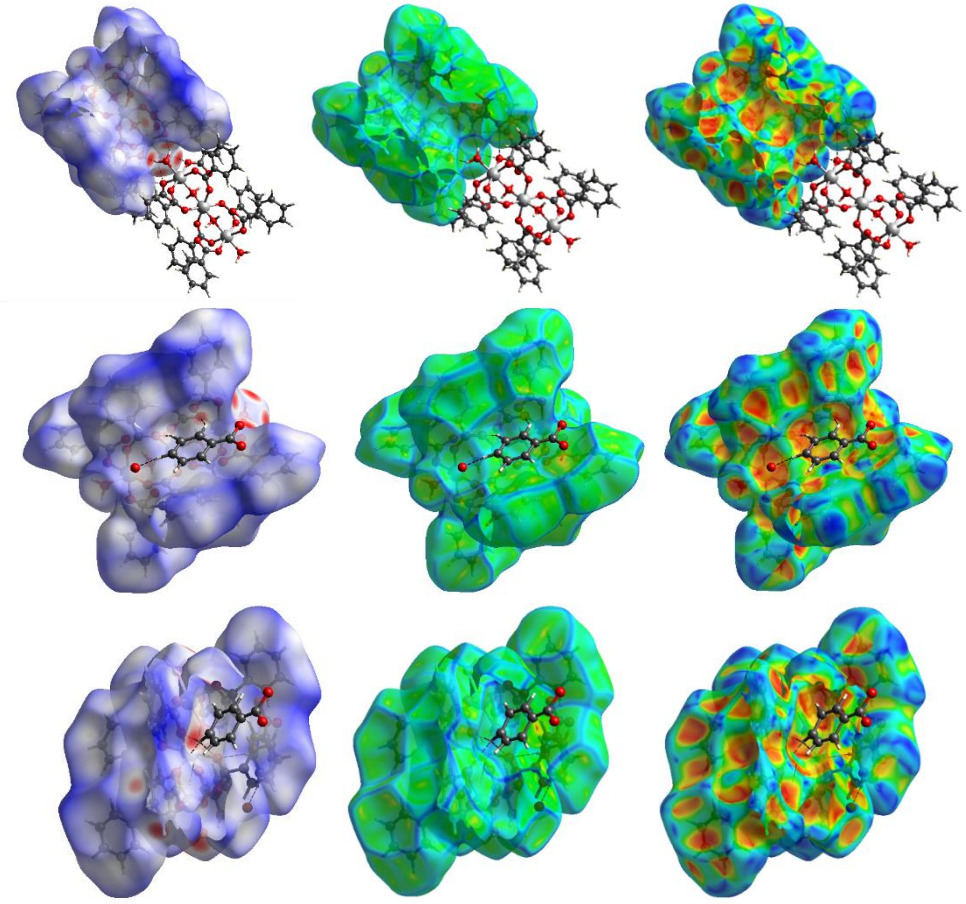

Figure 7. Views of the Hirshfeld surfaces mapped over d_{norm} (left), Curvedness (middle), and Shape index (right), highlighting different intramolecular contacts for (a) complex $[Co(Isoq)_4Cl_2]$ **1** , (b) complex $[Co_2(DMPA)_2(\mu\text{-}Benz)_4]$ **2** and (c) complex $[Co_3(Benz)_4(\mu\text{-}Benz)_4.(H_2O)_4]$ **3**

The molecular structure of complex **1** exhibits intense circular depression (deep red) on the Hirshfeld surface, which are mapped over d_{norm} (Figure 7-a). The depressions indicate H···Cl and C···H contacts namely H17···Cl4 (2.702 Å), H47···Cl2 (2.855 Å), C3···H68 (2.708 Å), C34A···H43 (2.650 Å), C33A···H43 (2.646 Å), C47···H31A (2.800 Å), C48···H30A (2.726 Å), and C49···H30A (2.794 Å). The small extent of area and light colour on the surface reveal weaker and longer contacts. On the structure of complex **2**, the deep red spots mapped over d_{norm} (Figure 7-b) represent O2···H11 (2.584 Å) and H12···H10 (2.291 Å) contacts. These contacts are illustrated on the Hirshfeld surface mapped with the shape-index property by orange and green regions, respectively. Complex **3** displays strong H-bonding interactions, which are evident from its Hirshfeld surface mapped over d_{norm} (Figure 7-c). The directional contacts are also defined also by deep red spots and are presented in three different levels. The first level is mainly distributed between the external water molecule (-O20H_2) and bridged benzoate's oxygen; O15···H1T (2.073 Å), O17···H2T (2.062 Å), O5···H3T (2.119 Å), and O7···H4T (2.013 Å). The second and the third levels concern the contacts of two non-coordinated benzoate's hydrogen atoms separately toward the bridged benzoate through their oxygens. Referring to the contact distances (Supporting information) and the colour scale of spots, from deep-red to faint-red, it suggested that contact O1···H68B (1.929 Å) is the most important H-bonding interaction. Then comes O6···H59 (2.343 Å), O8···H68B (2.579 Å), O3···H60 (2.611 Å), and finally O3···H68B (2.760 Å), respectively. All the blue and bright-orange surfaces around atoms and rings presented with shape-index plots correspond to the intermolecular interactions between the spherical orbital of the hydrogen atom and p orbitals of the benzoate rings (maximum overlap of the aromatic ring): H19···(C_{51-56}), H20···(C_{51-56}), H12···(C_{30-34}), H48···(C_{23-28}), H49···(C_{23-28}), H5···(C_{9-14}), and H6···(C_{9-14}). The associated 2D fingerprint plots (Supporting Information) point out that the H···H interactions, depicted by a central spike, are the major contributors to the crystal stability of complexes (**1**-**3**), comprising 49%, 49.6%, and 47% of the total Hirshfeld's surface, respectively. Additionally, the C···H/H···C contacts accounted for 34%, 36.4%, and 31.6% of the total surface in the same order as above, appearing as a pair of wings in the 2D plot. The stability of the compounds **2** and **3** is mainly due to the formation of intramolecular hydrogen bonding via H···O/O···H contacts, which makes up 11.3% and 14.1% in **2** and **3** complexes, respectively. The difference between these percentages is due to the O···H contacts provided by coordinated bridged or non-bridged water molecules. This is obviously supported by the contribution of the free water

RESEARCH ARTICLE

molecule that binds the crystal units and oxygen atoms of the bridged benzoate ligands. Complex **1** shows a low percentage (2.2%) of H···O/O···H contacts, which refer to the water molecule that binds two complex units, highlighted in the three-dimensional d_{norm} surface as deep red circular spots near the hydrogen atoms of the isoquinoline. The presence of these short-range interactions makes the formed complexes more stable [50–52]. Furthermore, some other interactions with a minor quantitative contribution to the crystal packing sustainability are noticed depending on the unit's structure. Their contributions in the complexes are given as follows **1**: C···C (5.5%), H···N/N···H (0.1%), Cl···O (0.5%) and Cl···H/ H···Cl (8.7%). In the complex **2**: C···C (0.7%), H···N/N···H (1.5%), C···N/N···C (0.5%), and N···N (0.1%). In the complex **3**: C···C (2.7%), C···O (3.3%), and O···O (1.5%). The quantitative results of the Hirshfeld surface analysis are depicted in Figure 8.

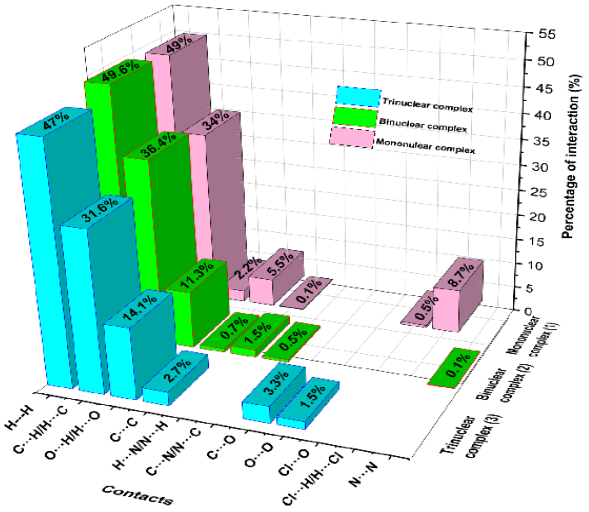

Figure 8. Percentage contributions of interatomic contacts to the Hirshfeld surface for the obtained complexes (**1**–**3**)

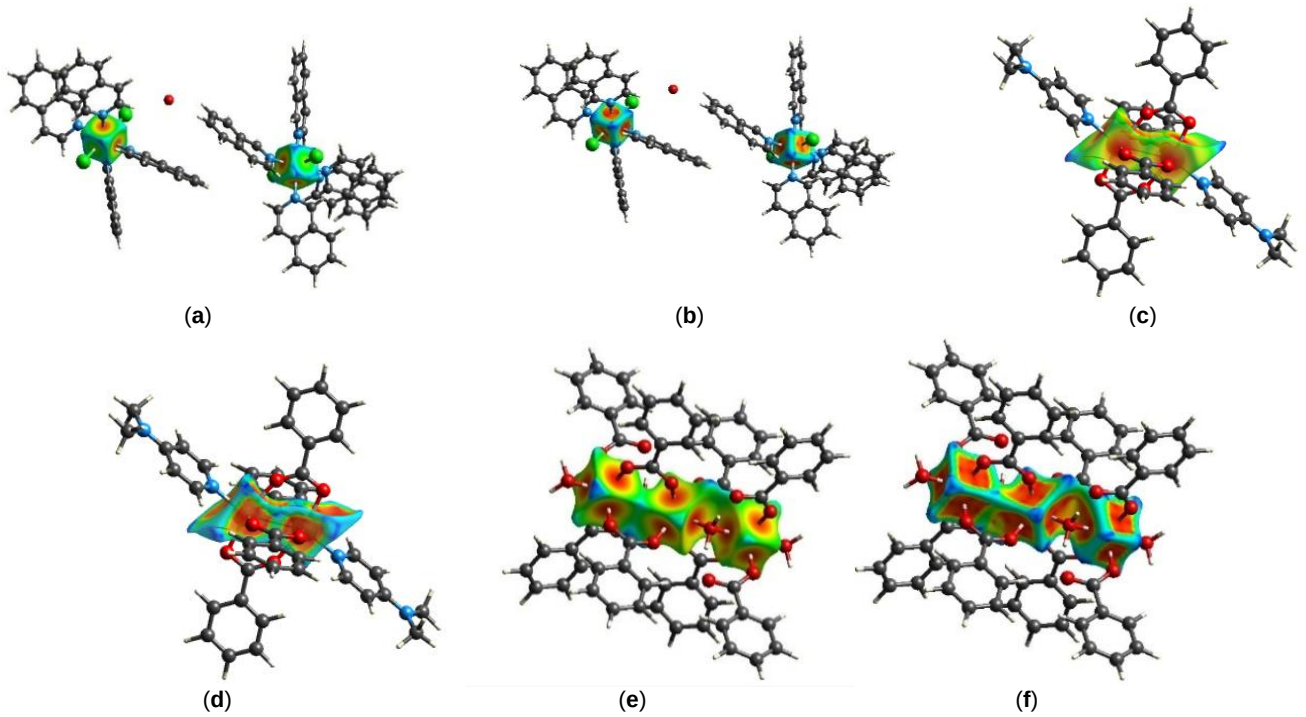

Figure 9. View of the Hirshfeld surfaces calculated for the cobalt (II) centres alone, highlighting the coordination geometries formed by the coordination sites of the donors sets mapped over: (**a**) the distance d_e external to the surface in the range 1.013 to 1.750 Å for **1**, (**c**) the distance d_e external to the surface in the range 0.985 to 2.179 Å for **2**, and (**e**) the distance d_e external to the surface in the range 0.992 to 1.990 Å for **3**. All the complexes show a Shape-index (S) from -1.0 to +1.0 (a.u) (**b, d, f**)

To confirm that complexes **(1-3)** have similar geometry, it was interesting to calculate the Hirshfeld surfaces of the individual metal centres. The 2D fingerprints shown in Figure 9 only consider the HS around the metal atoms and reflect the different coordination geometries around the metal centres. In complex **1**, the cobalt (II) ion exhibits a distribution of two parallel aligned red dots for $d_e + d_i$ ~ 1.6 Å (both lower and upper portion) of the coordinated bonds Co–N (62.6%) and Co–Cl (24.9%), respectively, with approximately the same slopes and d_e (Co–Cl) > d_e (Co–N) (Figure 10-a). In the metal centre in (**2**) 2D fingerprint, the distribution of aligned red dots for $d_e + d_i$ ~ 1.6 Å (upper portion) and $d_e + d_i$ ~ 1.4 Å (lower portion) for Co–N and Co–O bonds, respectively, have a slightly different slope (Figure-10-b), leading to a slightly deformed geometry. The Co–O (69.6%) bonds are more dominant than the Co–N (18.8%), with a weak area of contact attributed to H···Co interactions at (11.6%) (Figure 10-b).

RESEARCH ARTICLE

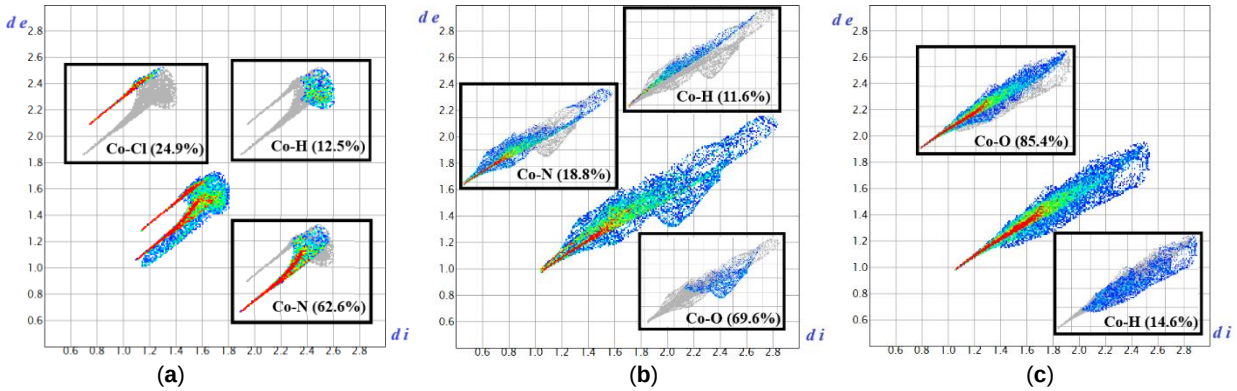

Figure 10. The two-dimensional fingerprint plots considering only the Hirshfeld surface of the cobalt (II) centre for (**a**) complex $[Co(Isoq)_4Cl_2]$ **1**, (**b**) complex $[Co_2(DMPA)_2(\mu\text{-}Benz)_4]$ **2** and (**c**) complex $[Co_3(Benz)_4(\mu\text{-}Benz)_3.(H_2O)$

The deformed 3D Hirshfeld surface map on the N1–Co–O4 region, confirms the difference in Co–O and Co–N bond lengths values at this level. Theoretically, it is explained by the similar electronegativity values of oxygen and nitrogen atoms. Above all, when they are situated on perpendicular plans (see SCXRD), which in turn causes strong repulsive energy and deformed coordination geometry. In the Cobalt region of the trinuclear crystal (**3**), the 2D fingerprint plots of the interatomic interactions indicate that the Cobalt atom has up to 85.4% of the contacts from the Co–O interactions, and the remaining 14.6% from H···Co contacts. The aligned red dots superimposed for $d_e + d_i$ ~1.7 are due to the symmetric coordination geometry (Figure-10-c).

THERMAL BEHAVIOUR

To characterise isolated solid complexes (**1**-**3**) and to shed some light on their thermal stability, thermogravimetric analysis coupled with differential scanning calorimetric analysis (TGA-DSC) was conducted by increasing the temperature at a rate of 10 °C/min, from ambient up to 600 °C under nitrogen atmosphere. The obtained thermograms are given in Figures 11-a, 11-b, and 11-c (For more details on the decomposition steps see supporting information). All the decomposition steps were exhibited by fusion followed by evaporation; suggesting that there was no oxidative degradation of the complexes. The TGA thermogram of compound **1** showed four stages of decomposition. The first stage occurred in the temperature range of 96-189 °C, showing a mass loss of 16%. This was due to the removal of superficial water molecules, with the percentage being slightly higher than usual due to storage conditions. The above loss was accompanied by a strong endothermic peak at 157 °C in the DSC curve. The second stage occurred in the temperature range 189-283°C and was due to the dehydration of compressed and co-crystallised water found in the internal crystal mesh, resulting in a mass loss of 25%. According to the literature [53,54], the $CoCl_2$ salt is thermally very stable and could not decompose easily under 600 °C. Therefore, the decomposition steps under this temperature correspond to the removal of the organic moieties. The anhydrous complex continued to decompose rapidly at temperatures ranging from 350 to 420 °C due to the decomposition of Co–N bonds and loss of the isoquinoline free radicals ($^{\cdot}C_9H_7N$). This was confirmed by the total mass loss of 40%. Finally, it has been observed that metal oxides such as CoO, Co_3O_4, or Co_2O_3, as well as $CoCl_2$, can remain as residual components in the temperature range of 420 to 580 °C. These components can make up to 20% of the final residue and this phenomenon depends on both the oxidation state and specific reaction conditions [55,56]. The mixed ligand Co^{II} complex (compound **2**) displays two steps of thermal decomposition in addition to the dehydration step process of crystallised water molecules, with a mass loss of 2%, this is taken place at the temperature ranging from 133 to 169 °C, matching with an endothermic peak at 152 °C. In the temperature range of 170-269 °C, the anhydrous complex remains stable. Above this range, the N, N-dimethyl-4-aminopyridine (DMAP) moieties begin to degrade between 269 and 306 °C, followed by an endothermic peak at 287 °C, which causes a mass loss of 4% at 289 °C. This may be due to the fact that the DMPA ligands have the lowest abundance toward the benzoates, which represent 2/3 of the ligands in the present structure, and the benzoates have a higher thermal stability than the DMAP. The next stage is in the range of 306-456 °C, with an endothermic peak on the DSC curve at 390 °C. This is due to the melting process during the decomposition of the benzoate ligands through the fragmentation of the Co–O bonds, which results in mass loss of 78 %. The residual mass (16%) may also be due to the cobalt oxides. Complex **3** shows four endothermic peaks in the DSC curve at 96, 129, 265, and 391°C. The first mass loss occurs at 88 °C, corresponding to the release of non-coordinated water molecules, which is consistent with the single-crystal structure. The second stage of decomposition arises in the range of temperature of 104-154 °C, resulting in a 6% of weight loss, and refers to the removal of coordinated water molecules in the crystalline structure (external and bridged water (see X–ray §). A strong endothermic peak is observed at 129 °C. In the temperature range of 210-290 °C, there is a mass loss (11%) accompanied by an endothermic peak at 265 °C. This can be attributed to the degradation of non-coordinated benzoates. At a higher temperature, there is one last decomposition step

RESEARCH ARTICLE

appearing on the TG curves in the temperature range of 291-469 °C. The weight loss becomes consistent at this stage making 64% of the total weight loss, due to the melting procedure during the decomposition of the benzoate ligands. Indeed, this is confirmed by an endothermic peak in the DSC plot at 392 °C and a maximum temperature of degradation (T_{max}) at 406 °C. A last small endothermic peak appears at 488 °C, without any mass loss, which may represent the melting point of the residual weight which is 17%. At this permanently stable stage, the composition of the residual mass can be attributed to the metal carbonate or metal oxide. Comparing the obtained results of the isolated complexes, it is noted that the trinuclear complex (**3**) is thermally less stable than the others. The loss of solvent molecules is observed at low temperatures of 70-103 °C (T_{max} = 88 °C) and 104-154 °C (T_{max} = 128 °C). On the other hand, the binuclear complex (**2**) showed high stability up to 280 °C, with solvent loss in the temperature ranging from 133 to 169 °C (T_{max} = 155 °C). Lastly, the mononuclear complex (**1**) is thermally stable up to 111°C and loses water molecules in the temperature range of 129 - 190 °C (T_{max} = 164 °C). All the residual masses of the complexes (**1**-**3**) remain almost constant until 600 °C under nitrogen gas.

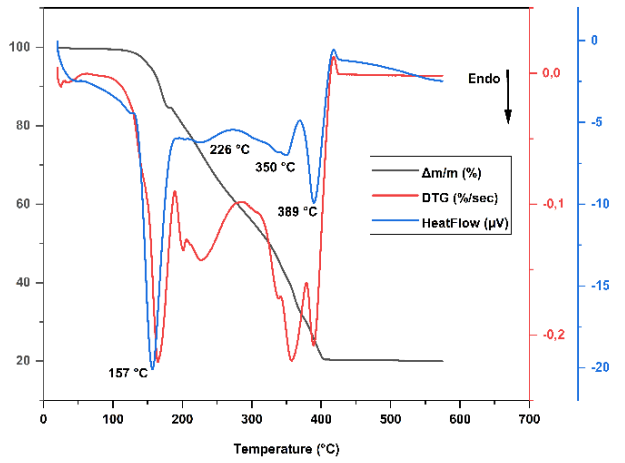

(**a**)

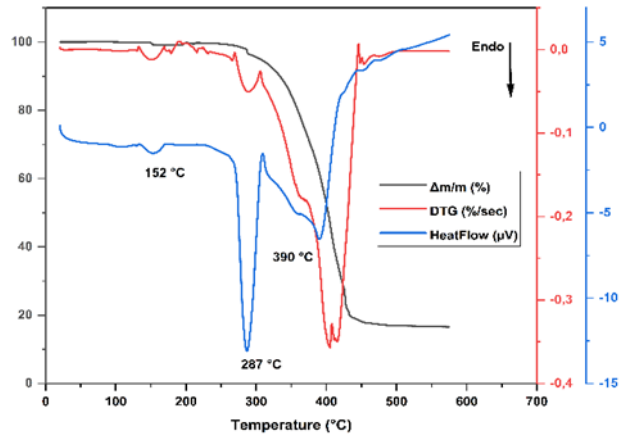

(**b**)

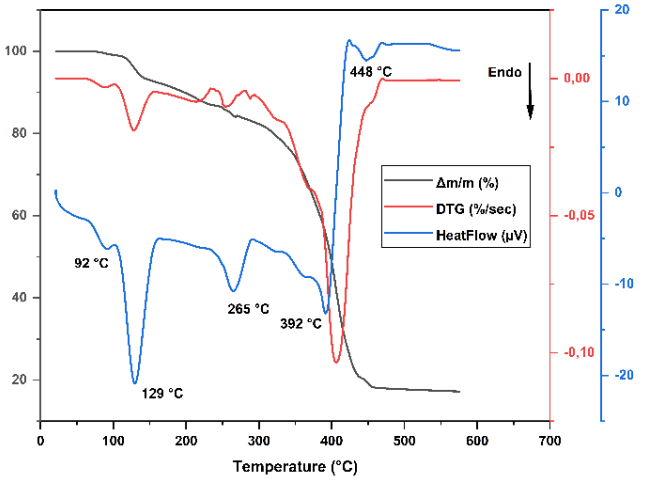

(**c**)

Figure 11. TGA-DTG-DSC curves of cobalt (II) complexes (**1**-**3**) where: (a) :**1**, (b): **2**, and (c): **3**

MAGNETIC SUSCEPTIBILITY

To estimate crystal-field parameters and exchange interactions of the Co^{II} ions in the synthesised compounds (**1**-**3**), magnetic susceptibility measurements were performed on single crystal samples in the temperature range of 2-300 K. The plots of the temperature dependence of the $\chi_M T$ product, where χ_M is the molar magnetic susceptibility, were analysed and Figures 12-a, 12-b, and 12-c show the results for **1**, **2**, and **3**, respectively. At room temperature (300 K), the compound **1** has a $\chi_M T$ value per formula unit of 4 cm^3 K mol^{-1}. This value is much larger than the expected spin-only value of 1.875 cm^3 K mol^{-1} for mononuclear cobalt (II) ion for three unpaired electrons in a high spin octahedral complex (S = 3/2, g = 2.0). The reason for this might be due to the larger g value (larger than 2.0) in cobalt (II) compounds and to a large orbital contribution that often observed in cobalt (II) octahedral complexes. Additionally, some ferromagnetic contribution of impurities might also be present [57]. Upon cooling, it gradually decreases until the $\chi_M T$ minimum is reached at 1.7 cm^3 K mol^{-1} at 2 K, with a slight increase at 10 K, which is found in some cases [58–60]. The slowdown below 80 K is attributed to the effect of magnetic anisotropy of the cobalt (II) ion rather than intermolecular interactions due to the long distances between the cobalt (II) ions [61]. The compound **2** has a $\chi_M T$ parameter value of 5.7 cm^3 K mol^{-1} at room temperature, which is also much larger than the spin-only value of 3.75 cm^3 K mol^{-1} for the dimer of the independent local S = 3/2 ions. This suggests a contribution of the orbital angular momentum [62]. The value of $\chi_M T$ also decreases gradually from room temperature to 50 K, and then it rapidly drops to its lowest measured temperature of 2 K with a value of $\chi_M T$ equal to 0.1 cm^3 K mol^{-1}. The data was fitted [63] as a dimer with spin Hamiltonian that describes the system as follows:

$$H = -J(S_{Co} \cdot S_{Co'})$$

where J is the super-exchange interaction parameter between cobalt (II) ions.

RESEARCH ARTICLE

According to the equation 2, The best fit according to equation 2 was obtained with g equal to 2.53 and an antiferromagnetic exchange interaction value *J* equal to -11.58 cm^{-1}. The fit plot, represented by a plain red line (Figure 12-b), was found to be in good agreement for temperature above 5K.

$$\chi = \frac{2N\beta^2 g^2}{kT}\frac{\exp\left(\frac{J}{kT}\right)+5\exp\left(\frac{3J}{kT}\right)+14\exp\left(\frac{6J}{kT}\right)}{1+3\exp\left(\frac{J}{kT}\right)+5\exp\left(\frac{3J}{kT}\right)+7\exp\left(\frac{6J}{kT}\right)} \quad \text{Eq.2}$$

$$\chi = \frac{N\beta^2 g^2}{3kT}\left[\frac{990}{4}\exp-\left(\frac{\frac{-99J}{8}+6J}{kT}\right)+126\exp-\left(\frac{\frac{-63J}{8}+6J}{kT}\right)+\frac{105}{2}\exp-\left(\frac{\frac{-35J}{8}+6J}{kT}\right)\right.$$
$$+15\exp-\left(\frac{\frac{-15J}{8}+6J}{kT}\right)+126\exp-\left(\frac{\frac{-63J}{8}+3J}{kT}\right)+\frac{105}{2}\exp-\left(\frac{\frac{-35J}{8}+3J}{kT}\right)$$
$$+15\exp-\left(\frac{\frac{-15J}{8}+3J}{kT}\right)+\frac{3}{2}\exp-\left(\frac{\frac{-3J}{8}+3J}{kT}\right)+\frac{105}{2}\exp-\left(\frac{\frac{-35J}{8}+J}{kT}\right)$$
$$\left.+15\exp-\left(\frac{\frac{-15J}{8}+J}{kT}\right)+\frac{3}{2}\exp-\left(\frac{\frac{-3J}{8}+J}{kT}\right)+15\exp-\left(\frac{\frac{-15J}{8}}{kT}\right)\right]\times$$
$$\left[10\exp-\left(\frac{\frac{-99J}{8}+6J}{kT}\right)+8\exp-\left(\frac{\frac{-63J}{8}+6J}{kT}\right)+6\exp-\left(\frac{\frac{-35J}{8}+6J}{kT}\right)\right.$$
$$+4\exp-\left(\frac{\frac{-15J}{8}+6J}{kT}\right)+8\exp-\left(\frac{\frac{-63J}{8}+3J}{kT}\right)+6\exp-\left(\frac{\frac{-35J}{8}+3J}{kT}\right)$$
$$+4\exp-\left(\frac{\frac{-15J}{8}+3J}{kT}\right)+2\exp-\left(\frac{\frac{-3J}{8}+3J}{kT}\right)+6\exp-\left(\frac{\frac{-35J}{8}+J}{kT}\right)$$
$$\left.+4\exp-\left(\frac{\frac{-15J}{8}+J}{kT}\right)+2\exp-\left(\frac{\frac{-3J}{8}+J}{kT}\right)+2\exp-\left(\frac{\frac{-15J}{8}}{kT}\right)\right]^{-1} \quad \text{Eq.3}$$

The compound **3** has a $\chi_M T$ value that decreases gradually from 9.2 cm^3 K mol^{-1} at room temperature as it cools down to a minimum value of 2.2 cm^3 K mol^{-1} at 2 K. The data was analysed by fitting it as a centrosymmetric trimer of S=3/2 spins using the spin Hamiltonian equation. The equation 3 was used to fit the data, which yielded a value of g = 2.64. The interaction between central cobalt (II) and each peripheral neighbour was calculated to be *J*=-9.16 cm^{-1} (See eq.3). The corresponding plot is given in plain red line in Figure 12-c.

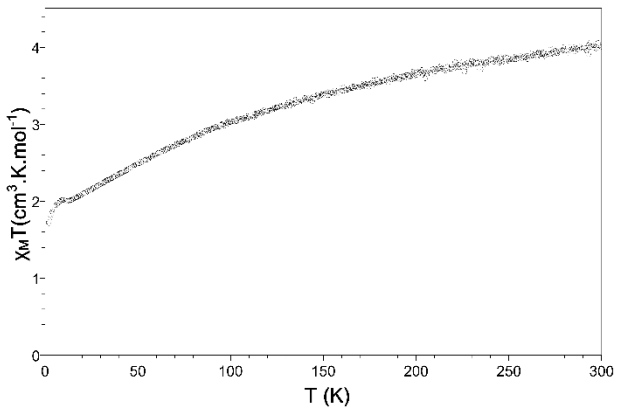

(**a**)

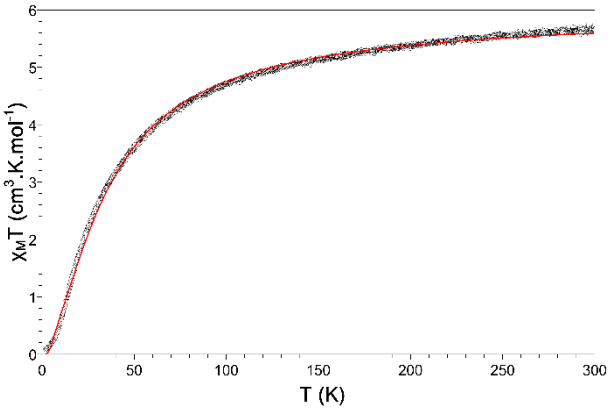

(**b**)

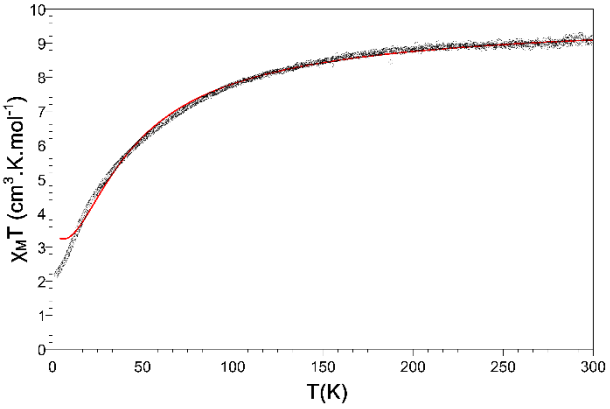

(**c**)

Figure 12. Molar magnetic susceptibility data for (a) complex **1**, (b) complex **2**, (c) complex **3** collected under an applied field of 0.1 T

FRONTIER MOLECULAR ORBITALS (FMOs)

FMO calculations are used to predict the chemical reactivity of molecules and explain their biological activities [54]. The interaction between HOMO and LUMO is a key factor in defining quantum chemical interactions. Their mechanism of action is known in DFT as electron charge transfer.

The difference in energy (ΔE) between these two energy levels results in the definition of the gap energy: $\Delta E = (E_{HOMO} - E_{LUMO})$. According to the maximum hardness principle [64,65], molecules with a large-gap are more stable than those with small-gap molecules. Small gap energy molecules are usually more polarizable [66].

10.1002/ejic.202400033

RESEARCH ARTICLE

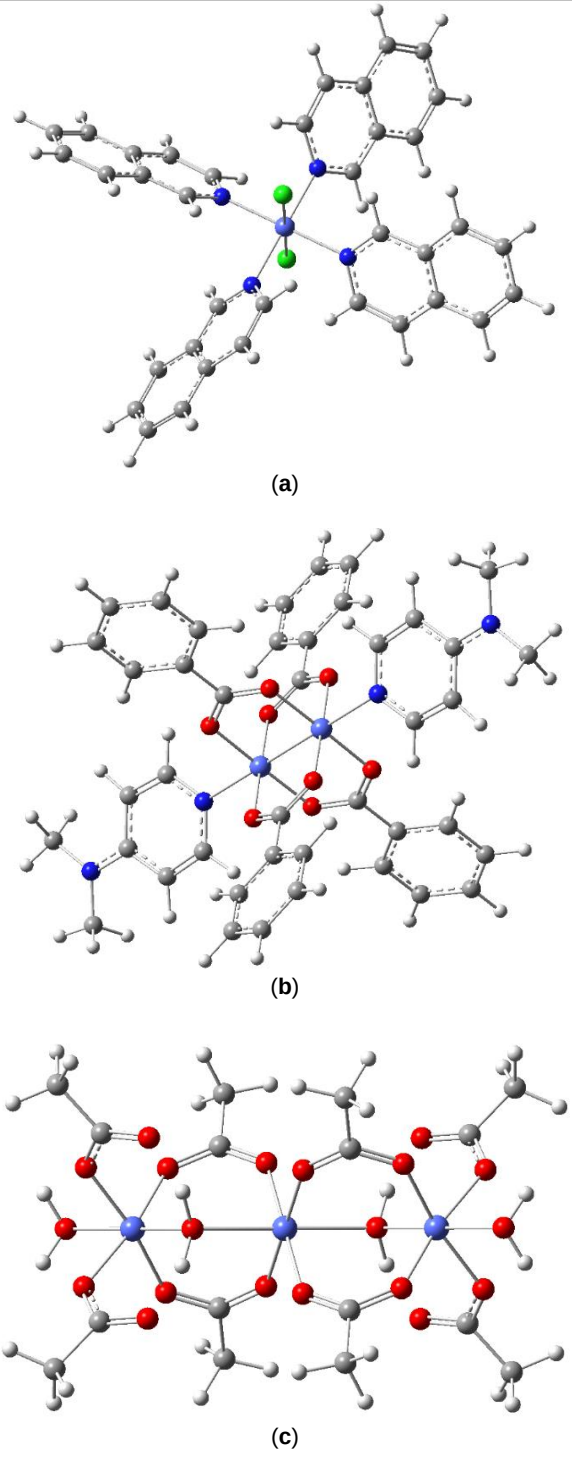

Figure 13. Optimized structures of complexes (**1**-**3**) obtained at B3LYP/6–311G(d,p) and LANL2DZ for cobalt (II) ions, where (a) :**1**, (b): **2**, and (c): **3**. The benzene cycles were replaced by the methyl groups for calculation purpose

The HOMO-LUMO gaps of compounds (**1**-**3**) were evaluated based on their optimised structures shown in Figures 13-a, 13-b, and 13-c. The corresponding shapes of the HOMO and LUMO orbitals are displayed in Figure 14. Upon analysing the results, it can be observed that the HOMO of compound **1** is mainly localised over metal and chloride atoms, while the LUMO is mainly delocalised to chloride and isoquinoline ligands. The nitrogen molecular orbitals overlap between each pair of isoquinoline, which contributes to Ligand→Metal (LM) and Ligand→Ligand (LL) charge transfer. Compound **2** exhibits Metal→Ligand charge transfer (MLCT) and metal-centred (MC) charge transfer. The HOMO is mainly located on the cobalt-cobalt bridge, cobalt ion, and the nitrogen atoms of the dimethyl aminopyridine moiety. The LUMO is delocalised along the whole molecular orbital of the benzoate ligand and cobalt ion. The HOMO of compound **3** is mainly localised over the middle cobalt atom and the oxygen atoms coordinated with it The LUMO is mainly delocalised over the external cobalt (Co3, $Co3^{ii}$) and oxygen water moieties (-O20H_2, -$O20^{ii}H_2$. The charge transfer occurring at this level is defined as Metal→Metal and Metal→Ligand charge transfer. Additionally, the results reveal that the presented complexes possess a relatively high ΔE gap energy, with corresponding values ranging in the 3.183 – 3.885 eV interval. Following the order **2** > **1** > **3**, it can be suggested that complex **3** has a more moderate chemical reactivity than both **1** and **2**.

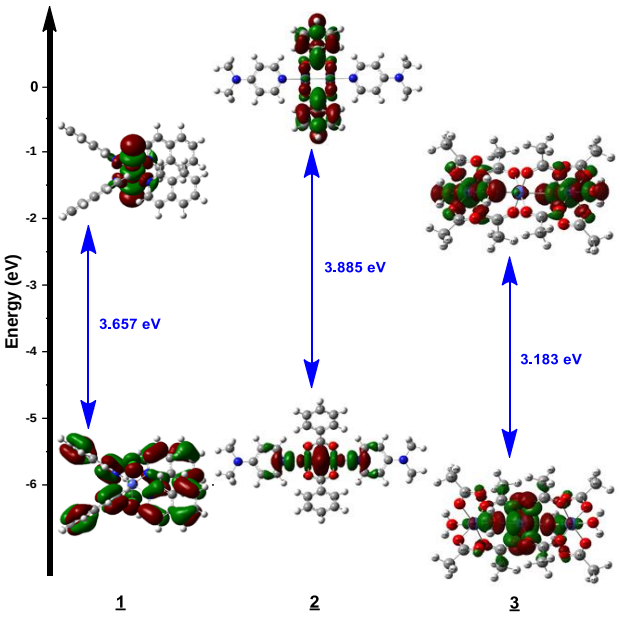

Figure 14. HOMO and LUMO diagram of the optimized structures (**1**-**3**) showing the distribution of electron density

NATURAL BOND ORBITAL (NBO) ANALYSIS

The intense interactions between electron donors and electron acceptors of the title structures (**1**-**3**) were evaluated by determining the higher stabilisation energies (E(2)). Due to the significant role of the delocalisation effect, the NBO study [67] was performed to investigate the interactions among bonds in coordination environments of cobalt (II) ions. The interactions between the filled lone pair donor NBOs of O, N, and Cl atoms and the empty metal hybrid orbitals were described as electron donation. The results of the study were determined and listed in supporting information. The NBO analysis showed that the first lone pair of nitrogen, the second lone pair of oxygen, and the

RESEARCH ARTICLE

fourth lone pair of chlorine atoms interacted with the anti-bonding NBOs of the cobalt ion, resulting in n/n* interactions. In complex **1**, the interaction energies between the metal ion and the chloride atoms are higher than those between the metal ions and the nitrogen atoms. The strongest electron donation comes from the lone pair orbital (LP) on chloride atoms, LP(4)Cl(13, 14) to anti-bonding acceptor LP*(4)Co2 orbitals. The energy E2 value was calculated as 77.85 kcal/mol. Therefore, the Co-Cl bonds are stronger than the Co-N bonds. Similarly, in Complex **2**, the interaction energy between the metal ion and the oxygen atoms is higher than that between the metal ions and the nitrogen atoms. The high energy E2 value was calculated as 29.45 kcal/mol, which corresponds to LP(2)O^{i}4→LP*(5)Co, LP(2) O^{i}3→LP*(5)Co^{i} LP(2) $O1^{i}$→LP*(5)Co^{i}, LP(2)O4→LP*(5)Co, LP(2)$O1^{i}$→LP* (5)Co^{i}, LP(2)O4→LP*(5)Co, LP(2)O3→LP*(5)Co, and LP(2)O2→LP*(5)Co^{i}. Thus, the Co-O bonds are stronger than the Co-N bonds. Finally, the NBO analysis of complex **3** reveals that the interaction energies between the central metal ion (Co3) and the coordination core atoms are greater than those between the metal ions (Co3 and $Co3^{ii}$) and their coordinating cores. The energy value E2 at the level of the central ion is of the order of 12 kcal/mol corresponding to LP(2)O13→LP*(5)Co4,LP(2)O13→LP*(6)Co4, LP(2)$O19^{ii}$→LP*(5)Co4,LP(2)$O19^{ii}$→LP*(6)Co4,LP(2)$O13^{ii}$→LP*(5)Co4, LP(2)$O13^{ii}$→LP*(6)Co4, LP(2)O12→LP*(5) Co4 and LP(2)O12→LP*(5)Co4. These bonds are stronger than those attributed to Co3-O and $Co3^{ii}$-O. Table 2 reports the natural electron configurations of cobalt atoms for the ground states of these complexes.

Table 2. Natural electronic configuration of the cobalt atoms in the studied compounds

Complex		Natural electron configuration
1	Co2	[core]4s(0.30)3d(7.38)4p(0.02)4d(0.01)
2	Co	[core]4s(0.34)3d(7.46)4p(0.03)
	Co^{i}	[core]4s(0.34)3d(7.46)4p(0.03)
3	Co4	[core]4s(0.13)3d(4.17)
	$Co3^{ii}$	[core]3d(3.60)4p(0.01)5s(0.14)
	Co3	[core]3d(3.60)4p(0.01)5s(0.14)

Complex **1** has an octahedral geometry containing a cobalt ion with a [d^7] configuration. By symmetry, the cobalt ion in complex **2** has the electronic configuration: Co [core]4s(0.34)3d(7.46)4p(0.03), suggesting a dimer with [d^7-d^7] configuration. Complex **3** confirms that the octahedral complex has a "d" shell-less occupied, and the Co^{ii} ions are in the [d^7-d^7-d^7] configuration. In complexes **1** and **2,** the Co configuration changes from d^7 to $d^{7.4}$ indicating a ligand-metal charge transfer. On the other hand, the cobalt configuration in compound **3** changes from d^7 to $d^{3.6}$ revealing a metal-ligand charge transfer.

GLOBAL REACTIVITY

Global reactivity descriptors such as ionisation energy (***IE***), electronic affinity (***EA***), electronegativity (***χ***), chemical potential (***μ***), global hardness (***η***), global softness (***S***), and global electrophilic index (***ω***) have been calculated for the studied compounds using the HOMO (π-donor) and LUMO (π-acceptor) formulas as defined in the literature [64,68–70]. The obtained results of the studied compounds are listed in Table 3. The reactivity parameters indicate that complex **2** has the lowest ionisation energy, which can be attributed to its electron-donating ability and highest antioxidant activity [71]. This observation is in good agreement with the experimental results. Moreover, it has been found that molecular stability correlates with hardness [65]. Compound **3** has lower hardness values compared to compounds **1** and **2**. This implies that the charge transfer process was more important in **3** than in **1** and **2**, suggesting that compound **3** has higher biological activity.

All complexes have electrophilic characteristics, and according to Domingo and Pérez [72], molecules with ω > 1.5 eV are strongly electrophilic moderate with 0.8 < ω < 1.5 eV, and marginal with ω < 0.8 eV. The results show that compounds **1** and **3** are highly electrophilic, which may contribute to the observed antioxidant activity, whereas compound **2** is a moderately electrophilic. This leads to the conclusion that the variation of basicity is as follows: **2** < **1** < **3**. According to Pauling's concept of electronegativity [73], the atoms in complex **3** have a greater power to attract electrons than in the other compounds (**1** and **2**), due to the presence of many oxygen atoms. This could be an additional effect on the binding affinity of bacteria proteins.

Table 3. Global reactivity descriptors of **(**1-**3)** complexes

	E_H (eV)	E_L (eV)	I (eV)	A (eV)	μ (eV)	χ (eV)	η (eV)	S (eV^{-1})	Ω (eV)
1	–5.525	–1.983	5.525	1.983	–3.754	3.754	3.542	0.284	1.989
2	–4.719	–0.834	4.719	0.834	–2.777	2.777	3.884	0.257	0.992
3	-5.658	-2.475	5.658	2.475	-4.067	4.067	3.183	0.314	2.598

Where:E_H: Energy of HOMO, E_L: Energy of LUMO. $I = -E_H$, $A = -E_L$, $\chi = -\mu = \frac{-1}{2}(E_L + E_H)$, $\mu = \frac{1}{2}(E_L + E_H)$, $\eta = (E_L - E_H)$, $S = \frac{1}{\eta}$, and $\omega = \frac{\mu^2}{2\eta}$

ELECTROSTATIC SURFACE POTENTIAL (ESP)

The ESP method allows the estimation of the reactivity of compounds to electrophilic and nucleophilic attacks [74–78]. In

RESEARCH ARTICLE

terms of colour scale, negative regions (red and yellow) are associated with high electron density, while positive regions (blue) are associated with electron defects. The green part represents the neutral zone. At this stage, the 3D plots of ESP maps of the title complexes (**1**-**3**) and the used ligands were performed on the same theoretical level as the optimisation.

The Electrostatic Potential (ESP) of ligands, including Isoquinoline, Benzoates, and Dimethylamino pyridine, was subjected also to analysis. The findings reveal that the nitrogen atoms within the aromatic systems (Figure 15), along with the oxygens, are identified as the most nucleophilic sites, playing a pivotal role in the complexation mechanism. Conversely, the hydrogen atoms within methyl groups and the peripheral aromatic hydrogens exhibit a relatively weak electrophilic character.

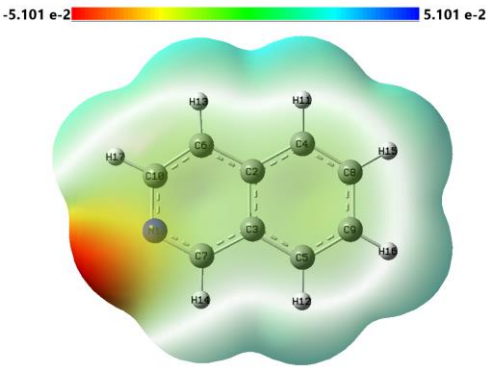

(a)

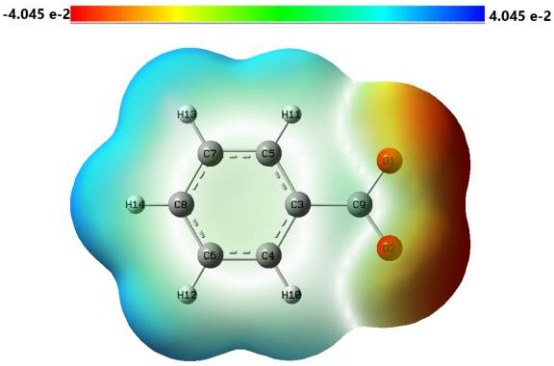

(b)

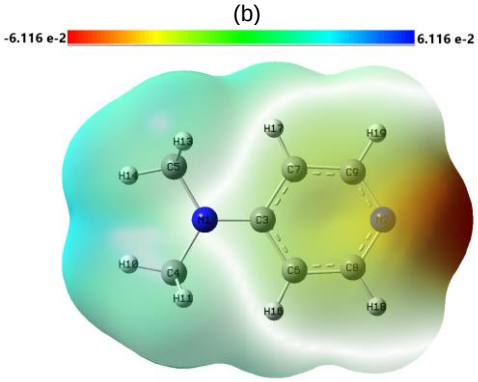

(c)

At the complexes level, the ESP results indicate that the neutral region with a potential close to zero is localised also around the aromatic systems (isoquinoline, DMAP, and benzoate). Negative regions are found on oxygen and chloride atoms. The positive areas were located on the peripheral hydrogens. Remarkably, minimal alterations were observed between ligand's plots and the corresponding complexes (**1**-**3**). The external -O20H_2 and -O20$^{ii}H_2$ groups of the complex **3** present the highest electrophilic character. These results also imply that these complexes could be deeply attracted by the positive molecular electrostatic potential of the studied micro-organisms.

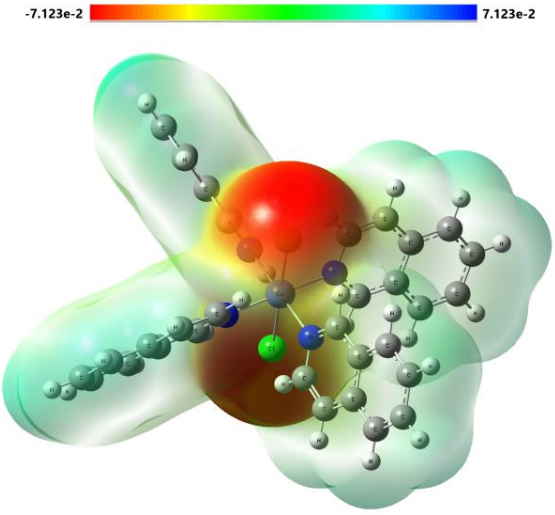

(d)

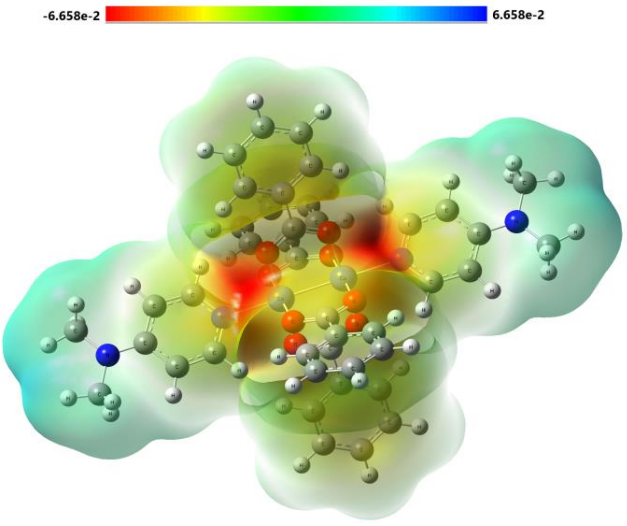

(e)

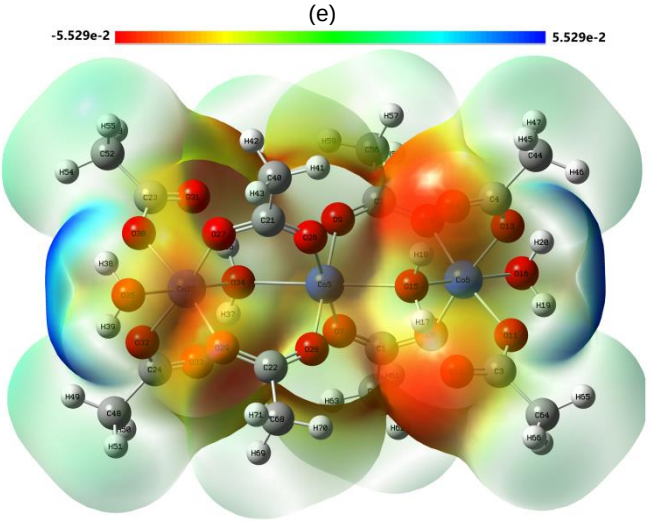

(f)

Figure 15. The molecular electrostatic potential surface of the ligands and the corresponding complexes calculated at the B3LYP/6-311G(d,p) level of theory

RESEARCH ARTICLE

IN-SILICO STUDY

GENERATION

The structures of the synthesised complexes (**1**-**3**) were depicted using a canonical simplified molecular input line entry system (SMILES) to estimate various in-silico pharmacokinetic parameters. The SMILES notations for these compounds were generated through the Open Babel GUI tool [79] and are presented in Table 4.

Table 4. Canonical Smiles of complexes (**1**-**3**)

Complex	Smiles
1	C1=C[C@H]2C=CC=CC2=CN1[Co](Cl)(Cl)(N1C=C[C@@H]2C=CC=CC2=C1)(N1C=C2C=CC=C[C@@H]2C=C1)N1C=C2C=CC=C[C@@H]2C=C1
2	[Co]1234(O[C@H](O[Co]2(O[C@@H](O1)c1ccccc1)(O[C@@H](O4)c1ccccc1)(O[C@@H](O3)c1ccccc1)N1C=C[C@H](N(C)C)C=C1)c1ccccc1)N1C=C[C@@H](N(C)C)C=C1
3	[C@H]1(c2ccccc2)O[Co@@]2(O[C@@H](c3ccccc3)O[Co](O1)(OC(=O)c1ccccc1)OC(=O)c1ccccc1)O[C@@H](c1ccccc1)O[Co](O[C@@H](c1ccccc1)O2)(OC(=O)c1ccccc1)OC(=O)c1ccccc1.O.O.O.O

TOXICITY STUDY

The pkCSM (Small-molecule pharmacokinetics prediction), is a machine-learning platform that has been instrumental in our analysis [80]. This platform is designed to predict small-molecule pharmacokinetic properties and relies on graph-based signatures to encode distance/pharmacophore patterns. The results are accessible at (https://biosig.lab.uq.edu.au/pkcsm/). The platform comprises 28 meticulously trained and validated regression and classification models that utilises diverse experimental datasets covering a comprehensive range of ADMET descriptors. These descriptors include predictions for various toxicities, namely Rat LD50, AMES toxicity, *Tetrahymena pyriformis* (*T. pyriformis*) toxicity, Minnow toxicity, Maximum Tolerated Dose, Oral Rat Chronic toxicity, Hepatotoxicity, and Skin sensitisation. The results of toxicological profiling of the newly synthesised complexes (**1**-**3**) provide a comprehensive assessment of acute and chronic toxicity, hepatotoxicity, skin sensitisation, and potential risks associated with hERG channel inhibition. Complex **1** demonstrates moderate acute toxicity (LD50 = 1.877 mol/kg) and potential toxicity to *T. pyriformis*. The AMES test confirmed that this compound is non-mutagenic, and it has a low toxic dose threshold in humans (MRTD = -0.781 log mg/kg/day). Complex **1** is not predicted to induce hepatotoxicity, though concerns arise regarding potential chronic toxicity (LOAEL = 1.078 log mg/kg_bw/day). Notably, it does not pose a risk of skin sensitization, but precaution is advised due to potential hERG II inhibition, suggesting cardiac risks. Complex **2** reveals moderate acute toxicity (LD50 = 2.482 mol/kg) and potential toxicity to *T. pyriformis*. Similar to complex **1**, it is non-mutagenic and has a moderate toxic dose threshold in humans (MRTD = 0.363 log mg/kg/day). While not predicted to induce hepatotoxicity, potential chronic toxicity concerns arise (LOAEL = 2.682 log mg/kg_bw/day). Complex **2** presents extremely high acute toxicity to Minnows, requiring a careful consideration. It also does not pose a risk of skin sensitisation, but safety use is needed due to the potential hERG II inhibition.

Table 5. The predicted results of various toxicities of complexes (**1**-**3**)

Model Name	Predicted Value			Unit
Complex	**1**	**2**	**3**	
AMES toxicity	No	No	No	Categorical (Yes/No)
Max. tolerated dose (human)	-0.781	0.363	0.438	Numeric (log mg/kg/day)
hERG I inhibitor	No	No	No	Categorical (Yes/No)
hERG II inhibitor	Yes	Yes	Yes	Categorical (Yes/No)
Oral Rat Acute Toxicity (LD50)	1.877	2.482	2.482	Numeric (mol/kg)
Oral Rat Chronic Toxicity (LOAEL)	1.078	2.682	-1.228	Numeric (log mg/kg_bw/day)
Hepatotoxicity	No	No	Yes	Categorical (Yes/No)
Skin Sensitisation	No	No	No	Categorical (Yes/No)
T. pyriformis toxicity	0.287	0.285	0.285	Numeric (log ug/L)
Minnow toxicity	-1.418	-6.658	-25.498	Numeric (log mM)

Complex **3** shares similarities with complex **2** in terms of moderate acute toxicity (LD50 = 2.482 mol/kg) and potential toxicity to *T. pyriformis*. It is non-mutagenic and has a moderate toxic dose threshold in humans (MRTD = 0.438 log mg/kg/day). Contrarily, complex **3** is predicted to induce hepatotoxicity, raising concerns for drug safety. Additionally, it exhibits extremely high acute toxicity to Minnows and potential chronic toxicity concerns (LOAEL = -1.228 log mg/kg_bw/day). Like the other complexes, it does not pose a risk of skin sensitisation, but precaution is warranted due to potential hERG II inhibition. The

RESEARCH ARTICLE

pkCSM predictions highlighted the potential pharmacokinetic and toxicity profiles of complexes (**1**-**3**). While encouraging in terms of AMES toxicity and Max. Tolerated dose, precaution is required due to the predicted hERG II inhibition and the varying results in chronic toxicity and hepatotoxicity.

PHYSICOCHEMICAL PROPERTIES

In this study, Lipinski's Rule of Five, a widely recognised set of guidelines predicting favorable drug-like properties, was applied to three distinct complexes denoted as **1**, **2**, and **3**. The rule postulates that compounds with less than 10 hydrogen bond acceptors (HBA), fewer than 5 hydrogen bond donors (HBD), a molecular weight below 500 Da (MW ≤ 500), and fewer than 10 rotatable bonds (nrotb ≤ 10) are more likely to exhibit good absorption or permeation [80]. Complex **1**, characterised by a molecular weight of 650.51 g/mol, exceeds the recommended threshold of 500 Da. However, it complies with Lipinski's Rule in terms of hydrogen bond acceptors (0), hydrogen bond donors (0), and rotatable bonds (4). These findings suggest that while complex **1** aligns with some aspects of Lipinski's Rule, its high molecular weight may pose challenges in terms of absorption and permeation. Complex **2**, with a molecular weight of 852.70 g/mol, surpasses the 500 Da, and the presence of 10 hydrogen bond acceptors raises concerns according to Lipinski's Rule. Despite meeting the criteria for hydrogen bond donors (0) and rotatable bonds (8), the complex's molecular characteristics may pose potential challenges in terms of bioavailability. Complex **3**, distinguished by a molecular weight of 1221.80 g/mol, significantly exceeds the 500 Da limit. With 20 hydrogen bond acceptors and 4 hydrogen bond donors, it surpasses Lipinski's Rule thresholds. Additionally, the presence of 16 rotatable bonds further raises concerns about its potential for absorption and permeation. The application of Lipinski's Rule of Five to the three complexes reveals varying degrees of adherence to the guidelines. While complex **1** exhibits some compliance, complexes **2** and **3** demonstrate molecular characteristics that may hinder their bioavailability. These findings provide valuable insights into drug development considerations, emphasising the importance of molecular properties in predicting the potential success of pharmaceutical compounds. Further experimental validation and refinement are recommended to comprehensively evaluate the bioavailability of these complexes.

Table 6. Some Physicochemical Properties of complexes (**1**-**3**)

	Physicochemical Properties		
	1	**2**	**3**
Formula	C36H32Cl2CoN4	C42H46Co2N4O8	C56H52Co3O20
Molecular weight	650.51 g/mol	852.70 g/mol	1221.80 g/mol
Num. heavy atoms	43	56	79
Num. arom. heavy atoms	0	24	48
Fraction Csp3	0.11	0.24	0.07
Num. rotatable bonds	4	8	16
Num. H-bond acceptors	0	10	20
Num. H-bond donors	0	0	4
Molar Refractivity	191.73	208.56	265.48
TPSA	12.96 Å²	86.80 Å²	215.96 Å²

Table 7. Drug-likeness profile of complexes (**1**-**3**)

	Druglikeness		
	1	**2**	**3**
Lipinski	No; 2 violations: MW>500, MLOGP>4.15	No; 2 violations: MW>500, Norb>10	No; 2 violations: MW>500, Norb>10
Ghose	No; 4 violations: MW>480, WLOGP>5.6, MR>130, #atoms>70	No; 4 violations: MW>480, WLOGP>5.6, MR>130, #atoms>70	No; 4 violations: MW>480, WLOGP>5.6, MR>130, #atoms>70
Veber	Yes	Yes	No; 2 violations: Rotors>10,

RESEARCH ARTICLE

			TPSA>140
Egan	No; 1 violation: WLOGP>5.88	No; 1 violation: WLOGP>5.88	No; 2 violations: WLOGP>5.88, TPSA>131.6
Muegge	No; 3 violations: MW>600, XLOGP3>5, #rings>7	No; 3 violations: MW>600, XLOGP3>5, #rings>7	No; 6 violations: MW>600, XLOGP3>5, TPSA>150, #rings>7, Rotors>15, H-acc>10
Bioavailability Score	0.17	0.17	0.17

BIOLOGICAL ACTIVITIES

The antimicrobial activity of cobalt (II) complexes **(1-3)** has been evaluated against six microbial strains and the findings are given in supporting information. The results of the antibacterial activity showed that all the tested complexes (**1**-**3**) and standards (penicillin and gentamicin) were biologically active against at least four bacterial strains. The metal complexes **2** and **3** revealed the highest activity against all the tested Gram-positive and Gram-negative strains. The highest zone of inhibition was detected in compound **3** against the strain *K. pneumoniae* with a value of MIC at 312.5 µg/mL. Good antibacterial activity was observed against all the tested bacterial strains with values of MIC ranging from 2.5 to 0.3125 mg/mL. However, all the tested metal complexes were less active compared to reference antibiotics. On the other hand, the fungal strain *C. albicans* displayed no activity against all the tested complexes. Furthermore, penicillin and gentamicin exhibited significant zones of inhibition against the tested bacteria ranging from 40 to 20 mm. Antibiotic resistance is currently one of the most serious threats to global health, food security, and social development. This phenomenon is caused by the misuse of antibiotics, whether treatments are too short/long or at inappropriate doses. As a result, an increasing number of infections, such as pneumoniae, tuberculosis or gonorrhoea, and salmonellosis, are becoming increasingly difficult to treat with classic antibiotics which lose their effectiveness. It is therefore essential to develop new and more practical approaches to combat these pathologies. The good antibacterial activity of the tested compounds **(1-3)** could be related to the polarity of the cobalt (II) complexes under coordination. Previous studies have shown that metal complexes are generally more active than ligands due to a reduction in polarity during coordination process [81–85]. This reduction is due to the overlapping of the bonding orbitals and the partial sharing of the positive charge of the metal ion with the donor groups. As a result, this greatly increases the lipophilicity of the metal complex allowing consequently the penetration of the complexes into the lipid membranes and causing damage to the respiratory process of cells [86]. Additionally, all the tested complexes are water-soluble displaying their compatibility with human physiological systems and their prospect for human pharmacology after *in vivo* cytotoxicity tests [87]. Cobalt (II) complexes have shown strong antibacterial activity against a range of Gram-positive and Gram-negative strains. This activity is due to their ability to disrupt the cell membrane or the electron transport chain of bacteria, leading to the production of reactive oxygen species (ROS) that can damage and ultimately kill the bacteria. A study conducted by Elaaraj and his colleagues [88] compared the antibacterial activity of the cobalt (II) complex of [2-(thiophen-2-yl)-1-(thiophen-2-ylmethyl)-1H-benzo[d]imidazole] ligand to that of the copper (II) and zinc (II) complexes. The results indicated that cobalt (II) complexes had the best antibacterial activity against the strains *Bacillus subtilis*, *Staphylococcus aureus*, *Pseudomonas aeruginosa*, and *Escherichia coli* compared to the other metal complexes. Similarly, in our previous work [32], the Di-µ-benzoato-bis [benzoatodipyridine-cobalt (II)] complex exhibited a high antibacterial activity against six bacterial strains. Additionally, many studies have been performed on the antibacterial activity of the cobalt (II) complex of curcumin, which have shown that the cobalt (II) complex of curcumin is more active than curcumin alone. This is because the cobalt (II) ion contributes to stabilising the complex and makes it more active and soluble in water, contributing also to its increased activity. Furthermore, the complex has a better safety profile than curcumin alone, as it is less likely to cause liver damage [89–91]. Also, many reports on the antimicrobial activity of cobalt (II) complexes with sulfanilamide derivatives have shown promising antimicrobial activity against a variety of Gram-positive/Gram-negative and fungi strains [92–97]. Irgi and his collaborators [98] indicated the potential antibacterial effect of cobalt (II) complexes with quinolone oxolinic acid, 2,2′-bipyridine, 2,2′-bipyridylamine, 1,10-phenanthroline, pyridine or 4-benzylpyridine ligands against Gram-negative (*E. coli* NCTC 29212 and *Xanthomonas campestris* ATCC 1395), and Gram-positive (*S. aureus* ATCC 6538 and *B. subtilis* ATCC 6633) bacterial strains.

In addition, cobalt (II) complexes based on a series of coordinated quinolone sparfloxacin with different co-ligands including methanol, 2,2′-bipyridine, 1,10-phenanthroline, and 2,2′-bipyridylamine showed that all the tested complexes had good antimicrobial activity against the strains *Escherichia coli*, *X. campestris*, *Staphylococcus aureus*, and *Bacillus subtilis* [99]. Also, the antibacterial activity of the cobalt (II), Nickel (II), Copper (II), Zinc (II), Cadmium (II), Mercury (II), Uranium (VI) oxide, and Thorium (IV) with isatin Schiff base against the strains *B. subtilis, S. aureus, E. coli, and P. aeruginosa* revealed that the cobalt (II) complex is the most active compared to the other tested complexes [100]. In contrast, Saghatforoush and his colleagues [101] mentioned that cobalt (II) complex with the unsymmetrical tetradentate Schiff bases, derived from amino thioether pyridine and salicylaldehyde derivatives, revealed higher activity against Gram-positive bacteria than those of Gram-negative bacteria, cobalt (II) complexes with sulindac and N-donor ligands were more effective against Gram-negative than Gram-positive bacterial strains [101]. Therefore, cobalt (II) complexes with various ligands such as imidazole, benzimidazole, curcumin, Schiff base, and sulfanilamide

RESEARCH ARTICLE

derivatives, possess strong antimicrobial properties. The potency of this activity can be influenced by the type of ligand, the metal ion's nature, and the type of tested bacterial strains. Interestingly, research has shown that cobalt (II) complexes are less harmful to human cells than free metal ions [102–104]. This finding suggests that cobalt (II) complexes could potentially be used as novel antibacterial agents with minimal toxicity concerns. However, further studies are needed to fully understand in detail the antibacterial efficacy of cobalt (II) complexes and assess deeply their safety for human use.

ANTI-INFLAMMATORY ACTIVITY

In vitro anti-inflammatory properties of cobalt (II) complexes **(1-3)** were tested through the assessment of their ability to inhibit ovalbumin denaturation and the findings are illustrated in Figure 16.

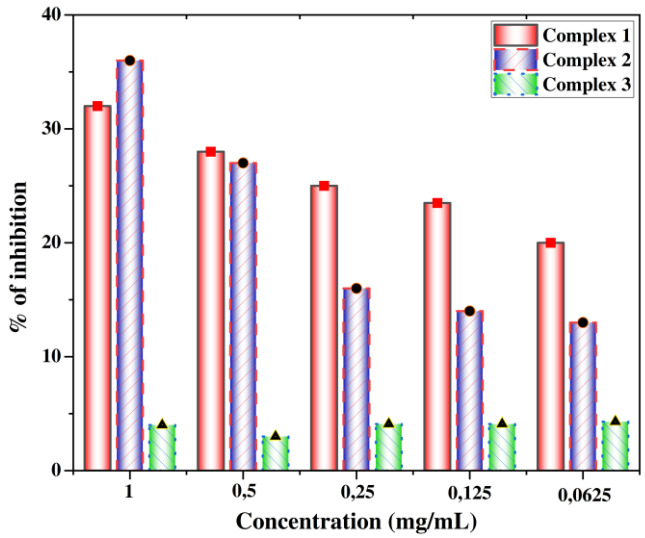

Figure 16. Anti-inflammatory activities of cobalt (II) complexes **(1-3)**

According to the obtained results, all the tested compounds **(1-3)** and the standard drug (diclofenac) prevent protein denaturation in a concentration-dependent manner. At the concentration of 1 mg/mL, compound **2** showed the highest anti-inflammatory effect with a percentage of inhibition at 35.23%, followed by compound **1** (30.92%) and finally compound **3** which exhibited the lowest anti-inflammatory activity at 2.71%. Moreover, all the tested metal complexes were less active than the reference drug which totally inhibited protein denaturation at the same tested concentration (IC_{50} at 163.75 ± 0.32 µg/mL). Denaturation of proteins is generated under the action of various physical and/or chemical agents that modify the electrostatic force, the hydrophobic and disulfide as well as the hydrogen bonds of proteins, affecting their solubility [105]. Denaturation of intracellular protein components is associated with tissue damage, leading to inflammation diseases like rheumatoid arthritis [106]. Therefore, there is clear evidence that the ability of drugs or synthetic compounds to inhibit protein denaturation has a potential anti-inflammatory activity [107]. Indeed, several studies have shown that many non-steroidal anti-inflammatory drugs such as diclofenac, ibuprofen, fenclofenac, and aceclofenac possess carboxylic acid groups in their structures causing gastric irritation [15,16]. Therefore, compound **3** exhibited the weakest anti-inflammatory effect with a value of 2.71% even though it contains seven carboxyl groups. This result could be explained by the covering of the carboxyl groups under the complex formation [108].

ANTIOXIDANT ACTIVITY

The antioxidant activity of cobalt (II) complexes (**1**, **2**, and **3**) and the references (BHT, BHA, ascorbic acid, and quercetin) was carried out spectrophotometrically using three different tests including DPPH radical scavenging assay, ferric thiocyanate method, and total antioxidant capacity. The results are given in Table 4. Indeed, all the tested compounds **(1-3)** act as antioxidants. In total antioxidant capacity, compounds **1** and **2** revealed strong antioxidant activities with values of 10.68 and 9.09 µg EAA/mg of complex, respectively. The results of ferric thiocyanate assay showed that compound **2** possesses a very strong antioxidant activity with a percentage of inhibition at 82.75 ± 0.75%, better than that of compounds **1**, **3**, BHA, quercetin, and ascorbic acid. However, this activity was slightly lower than that of the BHT (87.31 ± 0.27%) at the concentration of 100 µg/mL. Both compounds **1** and **3** displayed better antioxidant activity than BHA and quercetin at the same concentration. The highest antioxidant activity observed in ferric thiocyanate and the total antioxidant capacity could be explained by the polarity of the tested complexes. Indeed, the non-polar antioxidants can exhibit a stronger antioxidant power in emulsions because they concentrate in the lipid phase and the polar antioxidants remain in the aqueous phase and are therefore less effective in protecting lipids [109]. In the DPPH assay, at the concentration of 0.4 mg/mL, compounds **2** and **3** showed good antioxidant capacity with values of percentages of inhibition at 54.75 ± 0.56 and 32.53 ± 0.77 %, respectively. However, this activity is lower than that of the reference molecules. Several researchers have reported that the antioxidant activity of cobalt complexes is more active than ligands against the free radical DPPH [110–113]. This could be explained by the fact that the antioxidant activity of free ligands increases upon coordination with a metal ion, resulting in the acquisition of an additional metal centre for free radical scavenging by these compounds. This increases the ability of these molecules to stabilise unpaired electrons and thus scavenge free radicals.

In DPPH and FTC assays, strong positive correlation coefficients were observed between the tested complexes' inhibition percentages and the standard molecules with values of r = 0.769 and r = 0.665, respectively. These results indicated that the tested complexes (**1-3**) could act as antioxidant molecules. Moreover, a moderate correlation was detected between DPPH and FTC activities (r = 0,622), and a weak correlation coefficient was found between FTC and TAC activities (r = 0.412). In addition, a weak negative correlation coefficient was calculated between DPPH and TAC tests (r = -0.457). The obtained results could be linked to the tested mechanisms. Indeed, in the case of the DPPH test, both mechanisms including hydrogen transfer (HT) and electron transfer (ET) have been proposed [114]. These data could explain the negative correlation coefficient between the DPPH

and TAC assays, meaning that the complexes act with the hydrogen transfer (HT) mechanism in the DPPH test and with the electron transfer (ET) in the TAC assay.

Table 4. Results of antioxidant activities of cobalt (II) (**1**, **2**, and **3**) complexes and standards

	DPPH assay [a]	Ferric thiocyanate assay [a]	TAC assay [a]
Compounds and standards	IC50 (µg/mL)	% of inhibition	µg EAA/mg ex
1	ND	65.01 ± 1.14	10.68 ± 0.013
2	380.05 ± 0.26	82.75 ± 0.75	9.09 ± 0.043
3	ND	54.0 ± 0.32	7.29 ± 0.064
BHA[b]	6.82 ± 0.49	41.92 ± 0.43	NT
BHT[b]	22.32 ± 0.02	87.31 ± 0.27	NT
Ascorbic acid[b]	3.10 ± 0.002	61.86 ± 1.26	NT
Quercetin[b]	NT	46.07 ± 0.25	NT

[a]Values expressed are means ± SD of three measurements ($p < 0.05$), [b]Reference compounds, NT : Not tested, ND: Not detected.

Conclusion

This study describes the molecular structure, the chemical analysis and the biological evaluation of three novel cobalt (II) complexes; $[Co(Isoq)_4Cl_2]0.5H_2O$ (**1**), $[Co_2(DMPA)_2(\mu–Benz)_4]$ (**2**), and $[Co_3(Benz)_4(\mu–Benz)_4.(H_2O)_4]$ (**3**) having benzoate, isoquinoline, and dimethyl aminopyridine as ligands. The crystallographic analysis of the synthesised cobalt (II) complexes lays the foundation for understanding the molecular architecture of compounds **(1**-**3)**. Compound **1**, crystallising in the $P2_1/n$ space group, highlights specific molecular arrangements involving $[Co(Isoq)_4Cl_2]0.5H_2O$ complex and a water molecule in each asymmetric unit. The disorder in isoquinoline and the trans positioning of chlorides provide insights into its unique structure. Compound **2** crystallises in the centrosymmetric monoclinic $P2_1/n$ space group, revealing disorder in the dicobalt paddlewheel and influencing its coordination geometry. Compound **3**, crystallising in the centrosymmetric triclinic P-1 space group, displays distinctive arrangements of cobalt (II) trimers through inter-trimer hydrogen bond contacts. Building upon the structural insights, Hirshfeld surface analysis (HSA) and 2D fingerprint maps explore the molecular interactions and highlight key factors influencing the crystal stability of these complexes **(1**-**3)**. H···H interactions, constituting approximately 49-49.6% of the total HS, play a major role in stability across all complexes. Additionally, C···H/H···C contacts contribute significantly to their stability. The dimeric (**2**) and trimeric (**3**) complexes exhibit H···O/O···H intramolecular interactions accounting for 11.3% and 14.1%, respectively. This fluctuation is due to O···H contacts of water molecules. The mononuclear complex (**1**) displays a lower percentage (2.2%) of H···O/O···H contacts. Minor contributions of other interactions such as N···N, C···N, N···H, Cl···H, Cl···O, O···O, and C···O in crystal packing stability emphasise the complexity of intermolecular forces within each complex. Compound **1** exhibits strong hydrogen bonding points, while compound **2** displays specific contacts, and compound **3** showcases robust hydrogen-bonding interactions. These analyses provide a comprehensive understanding of intermolecular interactions, crystal packing, and metal coordination geometries in the synthesised complexes. The characterisation of thermal stability, as explored through TGA-DSC, complements further the structural information. Despite differences in thermal stability, all complexes maintain constant residual masses, and compound **3** shows comparatively lower thermal stability. This information adds a dynamic aspect to the understanding of the complexes' behaviour under varying temperature conditions. Moving to magnetic susceptibility measurements insights into crystal-field parameters and exchange interactions of cobalt (II) ions are gained. Compounds display a paramagnetic exchange interaction. In compound **1**, $\chi_M T$ decreases slowly, while compounds **2** and **3** exhibit a gradual decrease in magnetic susceptibility. These magnetic properties provide additional layers of knowledge regarding the electronic structure and interactions within the synthesised compounds. Transitioning to DFT calculations, Frontier Molecular Orbitals (FMOs) and Natural Bond Orbital (NBO) analyses predict the chemical reactivity and bonding interactions of compounds **(1**-**3)**. The results suggest unique charge transfer mechanisms, providing deeper insights into the electronic properties of each complex. The global reactivity descriptors calculated using HOMO and LUMO energies, emphasising different degrees of ionisation energy, electron-donating ability, and electrophilicity among the complexes. This improves further our understanding of the electronic properties and potential biological activities of compounds **(1**-**3)**. The application of the Electrostatic Potential (ESP) method relies the reactivity of compounds **(1**-**3)** to potential electrophilic and nucleophilic attacks. ESP maps offer insights into reactivity patterns and interactions with biological entities. Moreover, the antimicrobial, anti-inflammatory, and antioxidant assessments on the synthesised complexes **(1**-**3)** demonstrate the multifaceted potential of the investigated compounds in combating infections, inflammation, and oxidative stress. All the tested compounds **(1**-**3)** exhibited a strong antioxidant activity in ferric thiocyanate assay and total antioxidant capacity, and a moderate antioxidant activity in DPPH free radical scavenging method. Furthermore, compounds **(1**-**3)** showed an antibacterial effect against at least four bacterial strains and could prevent protein denaturation in a dose-dependent manner. Finally, the pkCSM predictions highlight the potential pharmacokinetic and toxicity profiles of complexes (**1**-**3**). While encouraging in terms of AMES toxicity and Max. Tolerated dose, safety measurements are needed due to the predicted hERG II inhibition, chronic toxicity, and hepatotoxicity. This comprehensive understanding, spanning from molecular structure to biological activity, underscores the promising therapeutic applications of the synthesised cobalt (II) complexes. Given these promising results, more *in vivo* investigation should be conducted to test these complexes and to support the discovery of new compounds to treat various incurable diseases.

RESEARCH ARTICLE

Supporting Information

The authors have cited additional references within the Supporting Information. [116-121]

Acknowledgments

The authors wish gratefully to express thanks to the DGRSDT and the Algerian Ministry of Higher Education and Scientific Research for PRFU Projects (**B00L01UN050120180007**, **B00L01UN050120230001,** and **B00L01UN050120230002).** X–Ray data collection was performed at the Centre de Diffractométrie X from the Institut des Sciences Chimiques de Rennes (UMR 6226 Université de Rennes – CNRS). SG thanks Dr. Thierry Roisnel for the data collection and Prof. Olivier Cador for magnetic fit. The authors gratefully acknowledge GENCI/CINES for HPC resources/computer time (Project cpt2130), and PSMN of ENS Lyon for computing resources

Keywords: Cobalt (II) complex • Thermal behaviour • DFT calculation • Magnetic susceptibility • Biological activity

References:

[1] C.R. Madzivire, P. Caramés-Méndez, C.M. Pask, R.M. Phillips, R.M. Lord, P.C. McGowan, Inorganica Chim Acta., **2019**, 498, 119025.
[2] T.A. Alorini, A.N. Al-Hakimi, S. El-Sayed Saeed, E.H.L. Alhamzi, A.E.A.E. Albadri, Arabian Journal of Chemistry., **2022**, 15, 103559.
[3] A. Abdou, J Mol Struct., **2022**, 1262, 132911.
[4] N. Benbellat, K.S. Gavrilenko, Y. le Gal, O. Cador, S. Golhen, A. Gouasmia, J.M. Fabre, L. Ouahab, Inorg Chem., **2006**, 45, 10440–10442.
[5] N. Benbellat, Y. le Gal, S. Golhen, A. Gouasmia, L. Ouahab, Synth Met., **2012**, 162, 1789–1797.
[6] V. V. Zyryanov, S.A. Petrov, A.S. Ulihin, Ceram Int., **2021**, 47, 29499–29503.
[7] B.N. Ameni, O. Abderrazek, R. Thierry, R. Walid, J Mol Struct., **2022**,1266, 133518.
[8] J.I. Melo, J.J. Phillips, J.E. Peralta, Chem Phys Lett., **2013**, 557, 110–113.
[9] S Dhamija, M Patra, J Pécaut, R Kataria, S Goswami, S Bhowmik, R Patra., Inorganica Chim Acta., **2022**, 535, 120852.
[10] Richa, A. Kumar, I. Verma, M. Gautam, R.D. Erande, J. Kłak, D. Choquesillo-Lazarte, A.J. Mota, A. Rajput, H. Arora, J Mol Struct.,**2022**, 133805.
[11] S. Belhouchat, S. Zeroual, N. Benbellat, O. Khaoua, S. Bouchekioua, R. Menacer, H. Chermette, ChemistrySelect., **2024**, 9, e202304155.
[12] C. Wang, B. Li, J. Ao, Food Chem., **2012**, 134, 1231–1238.
[13] N. Kumar, N. Goel, Biotechnology Reports., **2019**, 24, e00370.
[14] R. Sehrawat, P. Rathee, E.K. Akkol, S. Khatkar, A. Lather, N. Redhu, A. Khatkar, Curr Top Med Chem., **2022**, 22, 1472–1484.
[15] C. Dendrinou-Samara, G. Tsotsou, L. v. Ekateriniadou, A.H. Kortsaris, C.P. Raptopoulou, A. Terzis, D.A. Kyriakidis, D.P. Kessissoglou, J Inorg Biochem., **1998**, 71, 171–179.
[16] P. Emery, S.X. Kong, E.W. Ehrich, D.J. Watson, T.E. Towheed, Clin Ther., **2002**, 24, 1225–1291.
[17] F. Guenfoud, O. Khaoua, Z. Cherak, L. Loucif, W. Boussebaa, N. Benbellat, M. Laabassi, P. Mosset, J Mol Struct., **2024**, 1300, 137293.
[18] M. Alagumuthu, V.P. Muralidharan, M. Andrew, M.H. Ahmed, S.K. Iyer, S. Arumugam, Mol Inform., **2018**, 37, 1800048.
[19] A. Eskandari, A. Kundu, S. Ghosh, K. Suntharalingam, Angewandte Chemie., **2019**, 131, 12187–12192.
[20] Z. Wang, J. Li, G. Lin, Z. He, Y. Wang, Journal of Controlled Release., **2022**, 348, 1066–1088.
[21] W.A. Wani, S. Prashar, S. Shreaz, S. Gómez-Ruiz, Coord Chem Rev., **2016**, 312, 67–98.
[22] S. Parveen, F. Arjmand, S. Tabassum, Eur J Med Chem., **2019**, 175, 269–286.
[23] E. Giorgi, F. Binacchi, C. Marotta, D. Cirri, C. Gabbiani, A. Pratesi, Molecules., **2022**, 28, 273.
[24] A. Temesgen, H.C. Ananda Murthy, A.Z. Enyew, R. Revathi, R. Venkatesha Perumal, ChemistrySelect., **2023**, 8, e202302113.
[25] S. Dasari, P. Bernard Tchounwou, Cisplatin in cancer therapy: Molecular mechanisms of action, Eur J Pharmacol., **2014**, 740, 364–378.
[26] S. Okamoto, L.D. Eltis, Metallomics., **2011**, 3, 963–970.
[27] M.C. Heffern, N. Yamamoto, R.J. Holbrook, A.L. Eckermann, T.J. Meade, Curr Opin Chem Biol., **2013**, 17, 189–196.
[28] T.A.D. Smith, Bioorg Med Chem., **2005**, 13, 4576–4579.
[29] S. Tsiliou, L.A. Kefala, A.G. Hatzidimitriou, D.P. Kessissoglou, F. Perdih, A.N. Papadopoulos, I. Turel, G. Psomas, J Inorg Biochem., **2016**, 160, 125–139.
[30] K. Gałczyńska, K. Ciepluch, Ł. Madej, K. Kurdziel, B. Maciejewska, Z. Drulis-Kawa, A. Węgierek-Ciuk, A. Lankoff, M. Arabski, Scientific Reports., **2019**, 9,1–13.
[31] M. Muthuppalani, A. al Otaibi, S. Balasubramaniyan, S. Manikandan, P. Manimaran, G. Mathubala, A. Manikandan, M.N. Arshad, M. Puttegowda, H.S. Alorfi, A. Khan, A.M. Asiri, M.M. Rahman, Crystals., **2022**, 12, 326.
[32] O. Khaoua, N. Benbellat, S. Zeroual, S. Mouffouk, S. Golhen, A. Gouasmia, H. Chermette, H. Haba, J Mol Struct., **2023**, 1273, 134331.
[33] D. Sunmathi, R. Sivakumar, K. Ravikumar, International Journal of Advance Pharmaceutical and Biological Sciences., **2016**, 5, 109-115.
[34] M. S. Blois, Nature., **1958**, 181, 1199–1200.
[35] T. Takao, F. Kitatani, N. Watanabe, A. Yagi, K. Sakata, Biosci Biotechnol Biochem., **1994**, 58, 1780–1783.
[36] Z.Y. Yu, K.H. Lin, F.F. Zhang, M. Shao, M. Li, Acta Crystallogr Sect E Struct Rep Online., **2011**, 67, m206–m206.
[37] F.L. Hirshfeld, Theoretica Chimica Acta., **1977**, 44,129–138.
[38] M.A. Spackman, D. Jayatilaka, CrystEngComm., **2009**, 11, 19–32.
[39] H.F. Clausen, M.S. Chevallier, M.A. Spackman, B.B. Iversen, New Journal of Chemistry., **2010**, 34, 193–199.
[40] M.A. Spackman, J.J. McKinnon, CrystEngComm., **2002**, 4, 378–392.
[41] A. Parkin, G. Barr, W. Dong, C.J. Gilmore, D. Jayatilaka, J.J. McKinnon, M.A. Spackman, C.C. Wilson, CrystEngComm., **2007**, 9, 648–652.
[42] A.L. Rohl, M. Moret, W. Kaminsky, K. Claborn, J.J. McKinnon, B. Kahr, Cryst Growth Des., **2008**, 8, 4517–4525.
[43] S. Wolff, D. Grimwood, J. McKinnon, M. Turner, D. Jayatilaka, M. Spackman, Crystal Explorer, The University of Western Australia Perth, Australia **2012**.
[44] M.A. Spackman, P.G. Byrom, Chem Phys Lett., **1997**, 267, 215–220.
[45] J. J. McKinnon, A. S. Mitchell, M. A. Spackman, Chemistry A European Iournal., **1998**, 4, 2136–2141.
[46] F.L. Hirshfeld, Theoretica Chimica Acta., **1977**, 44, 129–138.
[47] M.A. Spackman, P.G. Byrom, Chem Phys Lett., **1997**, 267, 215–220.
[48] J.J. McKinnon, M.A. Spackman, A.S. Mitchell, Acta Crystallographica Section B: Structural Science., **2004**, 60, 627–668.
[49] R.B. Manawar, M.J. Mamtora, M.K. Shah, M.M. Jotani, E.R.T. Tiekink, Acta Crystallogr E Crystallogr Commun., **2020**, 76, 53–61.
[50] T. Lu, F. Chen, J Comput Chem., **2012**, 33, 580–592.
[51] L.L. Gan, H.Y. Niu, L. Le Liu, W.K. Dong, Y.J. Ding, J Mol Struct., **2024**, 1302, 137526.
[52] C.Y. Ma, X.X. Li, M.X. Du, W.K. Dong, Y.J. Ding, J Mol Struct., **2024**, 1298, 137071.
[53] S.K. Mishra, S.B. Kanungo, **1992**.
[54] D. Wu, Z. Tan, X. Feng, W.A. Anderson, Q. Li, Chemical Engineering Journal., **2017**, 315, 233–242.
[55] X.F. She, K. Zhu, J.S. Wang, Q.G. Xue, J Chem Res., **2022**, 46, 1.
[56] Z. Fan, Q. Sun, H. Yang, W. Zhu, F. Liao, Q. Shao, T. Zhang, H. Huang, T. Cheng, Y. Liu, M. Shao, M. Shao, Z. Kang, ACS Nano., **2024**, 18, 6, 5029–5039
[57] A. Laachir, F. Rhoufal, S. Guesmi, E.M. Ketatni, L. Jouffret, E. Kebir Hlil, N. Sergent, S. Obbade, F. Bentiss, J Mol Struct., **2020**, 1208, 127892.
[58] K. Chakarawet, P.C. Bunting, J.R. Long, J Am Chem Soc., **2018**, 140, 2058–2061.
[59] G.Z. Huang, Z.Y. Ruan, J.Y. Zheng, J.Y. Wu, Y.C. Chen, Q.W. Li, M.N. Akhtar, J.L. Liu, M.L. Tong, Science China Chemistry., **2018**, 61, 1399–1404.
[60] S. Zhang, L. Lu, J. Wang, X. Tan, B. An, A. Singh, A. Kumar, H. Sakiyama, J. Wang, Inorg Chem Commun., **2020** , 111, 107563.
[61] L. Chen, S.Y. Chen, Y.C. Sun, Y.M. Guo, L. Yu, X.T. Chen, Z. Wang, Z.W. Ouyang, Y. Song, Z.L. Xue, Dalton Transactions., **2015**, 44, 11482–11490.
[62] M. le Han, L. Bai, P. Tang, X.Q. Wu, Y.P. Wu, J. Zhao, D.S. Li, Y.Y. Wang, Dalton Transactions., **2015**, 44, 14673–14685.
[63] O. Kahn, Molecular magnetism. Courier Dover Publications., **2021**.
[64] H. Chermette, The Journal of Computational Chemistry., **1999**, 20, 129–154.
[65] R.G. Parr, P.K. Chattaraj, J Am Chem Soc., **1991**, 113, 1854–1855.
[66] A. B. Gündüzalp, N. Özbek, N. Karacan, Medicinal Chemistry Research., **2012**, 21, 3435–3444.
[67] E. D. Glendening, K.B. J, A. E. Reed, J. E. Carpenter, J. A. Bohmann, C. M. Morales, P. Karafiloglou, C. R. Landis, F. Weinhold, NBO 7.0, Theoretical Chemistry Institute, University of Wisconsin, Madison., **2018**.

[68] R.G. Parr, L. v. Szentpály, S. Liu, J Am Chem Soc., **1999**, 121, 1922–1924.
[69] R. G. Parr, R. A. Donnelly, M .Levy, & , W. E. Palke, J Chem Phys., **1978**, 68, 3801-3807.
[70] T. Koopmans, Physica., **1934**, 1, 104–113.
[71] F.I. Abouzayed, S.M. Emam, S.A. Abouel-Enein, J Mol Struct., **2020**, 1216, 128314.
[72] L.R. Domingo, P. Pérez, Org Biomol Chem., **2011**, 9, 7168–7175.
[73] K.S. Pitzer, J Am Chem Soc., **2002**, 82, 4121–4121.
[74] P Politzer, P R Laurence, K Jayasuriya, Environ Health Perspect., **1985**, 61, 191–202.
[75] J. S. Murray, P. Politzer, Wiley Interdiscip Rev Comput Mol Sci., **2011**, 1, 153–163.
[76] S. R. Gadre, C. H. Suresh, N. Mohan, Molecules., **2021**, 26, 3289.
[77] S. Lakshminarayanan, v. Jeyasingh, K. Murugesan, N. Selvapalam, G. Dass, J Photochem Photobiol., **2021**, 6, 100022.
[78] J. M. Campanario, E. Bronchalo, M. A. Hidalgo, J Chem Educ., **1994**, 71, 761.
[79] N.M. O'Boyle, M. Banck, C.A. James, C. Morley, T. Vandermeersch, G.R. Hutchison, J Cheminform., **2011**, 3, 1–14.
[80] D.E.V. Pires, T.L. Blundell, D.B. Ascher, J Med Chem., **2015**, 58, 4066–4072.
[81] E.L. Chang, C. Simmers, D.A. Knight, Pharmaceuticals., **2010**, 3, 1711–1728.
[82] A.M. Shalash, H.I. Abu Ali, Chem Cent J., **2017**, 11, 1–11.
[83] K.S. Abou-Melha, G.A. Al-Hazmi, I. Althagafi, A. Alharbi, F. Shaaban, N.M. El-Metwaly, A.A. El-Bindary, M.A. El-Bindary, J Mol Liq., **2021**, 334, 116498.
[84] V. Adimule, B.C. Yallur, V. Kamat, P.M. Krishna, J Pharm Investig., **2021**, 51, 347–359.
[85] M. Ghorbanpour, B. Soltani, O. Molavi, E.M. Aghdam, J Pharm Sci., **2022**, 28, 64–671.
[86] C.S. Dilip, K. Manikandan, D.R. Subahashini, R. Thiruneelakandan, J Chem., **2013**, 2013.
[87] G. Tamiru, A. Abebe, M. Abebe, M. Liyew, Ethiopian Journal of Science and Technology., **2019**, 12, 69–91.
[88] I. Elaaraj, S.E. Raouan, A. Nakkabi, B. Es-sounni, I. Koraichi, N. El moualij, M. Fahim, Journal of the Indian Chemical Society., **2022**, 99, 100404.
[89] K Girish, B.C Channu, D. Baba, Indian Journal of Pharmaceutical Sciences., **2019**, 81,1.
[90] A.K. Yadav, V. Singh, R. Kushwaha, D. Dolui, R. Rai, P. Dhar, A. Dutta, B. Koch, S. Banerjee, ChemBioChem., **2023**, 24, e202300033.
[91] T.J. Saritha, P. Metilda, Journal of Saudi Chemical Society., **2021**, 25, 101245.
[92] F. Blasco, L. Perelló, J. Latorre, J. Borrás, S. Garciá-Granda, J Inorg Biochem., **1996**, 61, 143–154.
[93] Ü.Ö. Özdemir, P. Güvenç, E. Şahin, F. Hamurcu, Inorganica Chim Acta., **2009**, 362, 2613–2618.
[94] H.G. Aslan, S. Özcan, N. Karacan, Inorg Chem Commun., **2011**, 14, 1550–1553.
[95] A. Ashraf, W.A. Siddiqui, J. Akbar, G. Mustafa, H. Krautscheid, N. Ullah, B. Mirza, F. Sher, M. Hanif, C.G. Hartinger, Inorganica Chim Acta., **2016**, 443, 179–185.
[96] M. Pervaiz, A. Riaz, A. Munir, Z. Saeed, S. Hussain, A. Rashid, U. Younas, A. Adnan, J Mol Struct., **2020**, 1202, 127284.
[97] S.H. Sumrra, A.U. Hassan, M. Imran, M. Khalid, E.U. Mughal, M.N. Zafar, M.N. Tahir, M.A. Raza, A.A.C. Braga, Appl Organomet Chem., **2020**, 34, e5623.
[98] E.P. Irgi, G.D. Geromichalos, S. Balala, J. Kljun, S. Kalogiannis, A. Papadopoulos, I. Turel, G. Psomas, RSC Adv., **2015**, 5, 36353–36367.
[99] E. Kouris, S. Kalogiannis, F. Perdih, I. Turel, G. Psomas, J Inorg Biochem., **2016**, 163, 18–27.
[100] K. Rama Krishna Reddy, P. Suneetha, C.S. Karigar, N.H. Manjunath, K.N. Mahendra, Journal of the Chilean Chemical Society., **2008**, 53, 1653–1657.
[101] L.A. Saghatforoush, F. Chalabian, A. Aminkhani, G. Karimnezhad, S. Ershad, Eur J Med Chem., **2009**, 44, 4490–4495.
[102] D.S. Raja, N.S.P. Bhuvanesh, K. Natarajan, Dalton Trans., **2012**, 41, 4365–4377.
[103] C.R. Munteanu, K. Suntharalingam, Dalton Trans., **2015**, 44, 13796–13808.
[104] K. Gałczyńska, K. Ciepluch, Ł. Madej, K. Kurdziel, B. Maciejewska, Z. Drulis-Kawa, A. Węgierek-Ciuk, A. Lankoff, M. Arabski, Scientific Reports., **2019**, 9, 1–13.
[105] G. Sangeetha, R. Vidhya, 31-International Journal of Herbal Medicine., **2016**, 4.
[106] N.I. Osman, N.J. Sidik, A. Awal, N.A.M. Adam, N.I. Rezali, J Intercult Ethnopharmacol., **2016**, 5, 343.
[107] D. Anokwah, E.A. Kwatia, I.K. Amponsah, Y. Jibira, B.K. Harley, E.O. Ameyaw, E. Obese, R.P. Biney, A.Y. Mensah, Heliyon., **2022**, 8, e10082.
[108] M. A Kale, R. Shelke, R. B Nawale, Formerly Current Medicinal Chemistry-Anti-Inflammatory and Anti-Allergy Agents., **2014**, 13, 36–44.
[109] I.I. Koleva, T.A. Van Beek, J.P.H. Linssen, A. De Groot, L.N. Evstatieva, Phytochemical Analysis, **2002**, 13, 8–17.
[110] N. Amiri, S. Nouir, M. Hajji, T. Roisnel, T. Guerfel, G. Simonneaux, H. Nasri, Journal of Saudi Chemical Society., **2019**, 23, 781–794.
[111] M. Aydın, E.H. Alıcı, A.T. Bilgiçli, M.N. Yarasir, G. Arabaci, Inorganica Chim Acta., **2017**, 464, 1–10.
[112] N. Söylemez, E. Yabas, S. Sahin Bolukbas, M. Sülü., **2018**, 22, 233–242.
[113] N. Yıldırım, A.T. Bilgiçli, E.H. Alici, G. Arabacı, M.N. Yarasir, J Mol Struct., **2017**, 1144, 66–79.
[114] İ. Gulcin, S.H. Alwasel, Processes., **2023**, 11, 2248.
[115] Deposition numbers 2255422 (for **1**), 2255421 (for **2**), and 2255423 (for **3**) contain the supplementary crystallographic data for this paper. These data are provided free of charge by the joint Cambridge Crystallographic Data Centre and Fachinformationszentrum Karlsruhe Access Structures service.

10.1002/ejic.202400033

RESEARCH ARTICLE

Entry for the Table of Contents

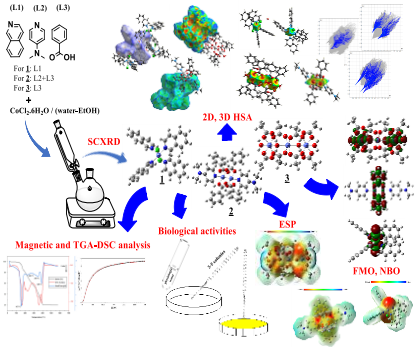

Three novel water-soluble cobalt crystals were synthesised and characterised. Structural, magnetic properties, and toxicity (pkCSM) profiles were analysed. The DFT method explored their reactivity, and NBO analysis revealed the coordination mechanisms. These compounds displayed strong antioxidant and antibacterial properties, indicating potential therapeutic uses. Additionally, the study assessed their anti-inflammatory effects.